DOI: https://doi.org/10.2138/am-2022-8118. http://www.minsocam.org/

Revision 2

Word Count: 7,718 (Word count including references: 10,909)

Pyrite geochemistry and its implications on Au–Cu skarn metallogeny: An example from the Jiguanzui deposit, Eastern China

Yu Zhang[1, 2, *], Huayong Chen[3, 4, 5], Jiamin Cheng[3], Jing Tian[3], Lejun Zhang[6], Paul Olin[6]

[1] Key Laboratory of Metallogenic Prediction of Nonferrous Metals and Geological Environment Monitoring (Central South University), Ministry of Education, Changsha 410083, China

[2] School of Geosciences and Info-Physics, Central South University, Changsha 410083, China

[3] Guangzhou Institute of Geochemistry, Chinese Academy of Sciences, Guangzhou 510640, China

[4] CAS Center for Excellence in Deep Earth Science, Guangzhou 510640, China

[5] Guangdong Provincial Key Laboratory of Mineral Physics and Materials, Guangzhou 510640, China

[6] Centre for Ore Deposits and Exploration Science (CODES), University of Tasmania, Hobart, Tasmania 7001, Australia

* Corresponding author: Y. Zhang (zyu2009@qq.com)

ABSTRACT

Trace element geochemistry of pyrite is widely used to monitor ore-forming processes of various types of deposits, but its application on skarn mineral systems is not well constrained due to the multistage nature and complex associated mineral assemblages for skarn-type pyrite. The Jiguanzui skarn Au–Cu deposit in the Middle–Lower Yangtze River Valley Metallogenic Belt (Eastern China) is characterized by abundant pyrite that formed in the main-ore (Py1), late-ore (Py2), and post-ore (Py3) stages, which makes it ideal for unravelling the skarn ore-fluid evolution. Specifically, Py1 is composed of quartz–pyrite (Py1a), quartz–calcite–pyrite (Py1b), quartz–sericite–pyrite (Py1c), quartz–chlorite ± epidote–pyrite (Py1d), and quartz–K-feldspar–pyrite (Py1e), among which Py1a is the most widespread. Py2 comprises calcite–pyrite (Py2a) and calcite–K-feldspar–pyrite (Py2b), and Py3 comprises bird's-eye pyrite (Py3a) and fingerprint-like pyrite (Py3b).

The varying Co/Ni ratios (mostly > 2) and coexistence with hydrothermal minerals (quartz, calcite, K-feldspar, chlorite, and epidote) reveal the hydrothermal origin of Py1 and Py2. The Co/Ni (0.97–7.30), Cu/Ni (8.94–186) and As/Ni (0.80–11.7) ratios, and the high trace element contents indicate that Py3a may have been genetically linked to the waning magmatic-hydrothermal system and increasing meteoric fluid influx. Py1 has generally higher Co-Ni-Se but lower Zn-As-Mo contents than Py2. Py1 in the orebodies has also higher Cu-Au contents than Py2, consistent with that Py1 was formed in the main Au–Cu ore stage. During the ore-fluid evolution, meteoric water input and abundant galena formation in the late-ore calcite-sulfide stage may have controlled the decreasing Se-Co-Ni contents from Py1 to Py2,

whilst the fluid cooling and pH rise (caused by the acidic fluid-carbonate rock reaction) may have increased the As-Zn-Mo contents from Py1 to Py2.

Py1a in the orebodies has higher As-Ag-Te but lower Co-Ni-Se contents than Py1a in the wallrocks. The decompression and phase separation (fluid boiling) by extensive hydraulic fracturing may have caused the higher temperature, pH and fO_2 for the Py1a-forming fluids in the orebodies (than those in the wallrocks). Such fluid physicochemical differences may have been the main controlling factor on trace element spatial variations of Py1a. More importantly, the spatial variation of these trace elements in Py1a provide insights for using pyrite trace element geochemistry in skarn mineral exploration.

Keywords: Pyrite geochemistry; Skarn Au–Cu system; Jiguanzui deposit; Middle–Lower Yangtze River Valley Metallogenic Belt; Eastern China

DOI: https://doi.org/10.2138/am-2022-8118. http://www.minsocam.org/

INTRODUCTION

Pyrite is one of the most abundant sulfide minerals on Earth and is the dominant metallic mineral in many hydrothermal ore systems (Deditius et al. 2011, 2014; Tanner et al. 2016). Owing to its stability under various physicochemical fluid conditions and sink capacity for many trace elements, including Co, Ni, Cu, As, Se, Mo, Ag, Sb, Te, Pb, Bi, Au and platinum group elements (PGEs), pyrite can effectively record the fluid changes in hydrothermal systems to constrain ore-forming processes (Fleet et al. 1993; Craig et al. 1998; Large et al. 2009; Smith et al. 2014; Tanner et al. 2016; Li et al. 2018a). Therefore, pyrite trace element geochemistry has been a focus of many gold deposit studies, including those of porphyry Cu–Au (e.g., Franchini et al. 2015), epithermal Au (e.g., Tanner et al. 2016; Sykora et al. 2018; Keith et al. 2020), orogenic Au (e.g., Cook et al. 2013; Gregory et al. 2016; Ward et al. 2017; Vote et al. 2019), Carlin-type Au (e.g., Large et al. 2009), and intrusion-related Au (e.g., Feng et al. 2020) type. However, pyrite from skarn deposits, one important source for global Au polymetallic resource (Meinert 1992; Zhang et al. 2018), lacks the same level of detailed study, possibly due to the often multiple generations of pyrite formation and complex coexisting mineral assemblages in skarn ore systems (Cromie et al. 2018).

The Jiguanzui Au–Cu skarn deposit, with a proven mineral reserve of 23.3 t Au @ 3.93 g/t and 0.16 Mt Cu @ 1.71% (Sun et al. 2019), is an important deposit in the Edong ore district of the Middle–Lower Yangtze River Valley Metallogenic Belt (MLYRB), Eastern China. Its remarkable feature is the extensive presence of multi-stage pyrite in various mineral assemblages in both orebodies and wallrocks (Tian et al. 2019), making it an ideal target for studying the Au-skarn ore

DOI: https://doi.org/10.2138/am-2022-8118. http://www.minsocam.org/

fluid evolution. Based on a large set of spatially and paragenetically well-constrained pyrite samples from Jiguanzui, this study has unraveled and discussed the trace element compositions of the different generations and types of pyrite from the various stages of ore formation. The analysis was based on laser ablation-inductively coupled plasma-mass spectrometry (LA-ICP-MS) trace element spot analysis coupled with back-scattered electron (BSE) imaging.

GEOLOGICAL SETTING

Regional geology

The MLYRB is known to host over 200 polymetallic deposits, which are clustered in seven ore districts, namely (from west to east): Edong, Jiurui, Anqing-Guichi, Luzong, Tongling, Ningwu, and Ningzhen. This belt is located along the northern edge of the Yangtze craton, and south of the Qingling-Dabieshan orogen and the North China craton. The MLYRB is predominantly confined by the NW-trending Xiangfan–Guangji fault, NE-trending Tancheng–Lujiang fault, and ENE-trending Yangxing–Changzhou fault (Fig. 1a; Pan and Dong 1999; Mao et al. 2011; Zhang et al. 2017a, b).

The Edong ore district forms the westernmost part of the MLYRB, and contains over 25 skarn Fe–Au–Cu–Mo deposits (Fig. 1b; Xie et al. 2011a). Sedimentary rocks exposed in the district are predominantly marine carbonate and clastic rocks, with ages spanning from the Cambrian to the Middle Triassic, among which the Triassic Daye Formation (Fm.) limestone and Puqi Fm. sandy-shale are closely skarn ore-related (Shu et al. 1992). Structurally, WNW-trending faults and folds are the major structures in the belt, and are inferred to have controlled the distribution of batholith emplacement and mineralization (Xie et al. 2008). Granitic batholiths are widely distributed in Edong, and the major six (Echeng, Tieshan, Jinshandian, Lingxiang, Yinzu, and Yangxin; Fig. 1b) cover an area of ca. 920 km^2 (approximately 21% of the Edong ore district; Duan and Jiang 2017). The Echeng (143–127 Ma; Xie et al. 2011b, 2012), Tieshan (142–136 Ma; Li et al. 2009; Xie et al. 2011b), and Jinshandian (133–127 Ma; Xie et al. 2012) batholiths are composed of quartz/biotite diorite, granite, and (minor) gabbro, and are space-time related to Fe skarn mineralization (Xie et al. 2011a). The Lingxiang (144–136 Ma) and Yangxin (142–138 Ma) batholiths (Li et al. 2009, 2010; Xie et al. 2011b) are dominated by quartz diorite-granodiorite, monzonite, and gabbro, and are space-time related to Cu–Fe(–Au) skarn mineralization (Xie et al. 2011a). The primarily-granodioritic Yinzu batholith (152–146 Ma), however, was generally considered to be not directly ore-related (Li et al. 2009, 2010).

Deposit geology

The Jiguanzui Au–Cu skarn deposit is located in the central part of the Edong ore district, near the northern and eastern margins of the Yangxin batholith and Jinniu basin, respectively (Fig. 1b). The local outcropping volcano-sedimentary sequences include mainly the Lower-Middle Triassic Jialingjiang and Puqi formations and the Cretaceous Majiashan and Lingxiang formations. The Jialingjiang Fm. dolomitic limestone was metamorphosed into dolomitic marble and is an important ore host, whereas the Puqi Fm. mudstone was metamorphosed into hornfels and is a secondary ore host. The Majiashan and Lingxiang formations contain mainly volcanic breccias. The NE-trending Jiguanshan thrust fault (F1) and NE-/NW-trending anticlines form the structural framework in the mining area. Local igneous rocks are dominated by quartz diorite of the Yangxin batholith (zircon U–Pb age: 139 ±1 Ma; Xie et al. 2011b), which crops out in the eastern Jiguanzui (Fig. 2a).

The Jiguanzui deposit is characterized by five economically significant NE-trending stratabound or lensoidal orebodies (I, II, III, IV, and VII), which are largely confined along the contact between the Jialingjiang Fm. dolomitic marble and the intruding quartz diorite. Orebodies I, II, III, and VII are NW-dipping at 50–74°, whereas orebody IV is SE-dipping at 13–76° (Ke et al. 2016). Additionally, some vein-type orebodies locally occur in the fracture zones of the Puqi Fm. hornfels (Fig. 2b). Based on detailed field geologic and petrographic observations, the major metallic minerals identified include magnetite, chalcopyrite, pyrite, galena, sphalerite, hematite, bornite, and native gold, which occur as massive, veins, or disseminations. Major non-metallic minerals include mainly calcic-silicates (e.g., garnet, pyroxene, hornblende, epidote, and actinolite), K-feldspar, chlorite, quartz, calcite, muscovite, illite, and montmorillonite (Tian et al. 2019; Zhang et al. 2019). Wallrock alteration at Jiguanzui includes mainly garnet, K-feldspar, pyroxene, sericite, quartz and calcite (Tian et al. 2019; Zhang et al. 2019). Zhang (2015) and Tian et al. (2019) divided the Jiguanzui mineralization into five stages based on mineral assemblages and textural relations (Fig. 3), i.e., (I) prograde skarn (garnet–pyroxene), (II) retrograde alteration (hornblende–epidote–actinolite), (III) hematite, (IV) quartz–pyrite–chalcopyrite (main Au–Cu ore stage), and (V) calcite–sulfide (pyrite–chalcopyrite–molybdenite–sphalerite–galena). Previous studies on the Jiguanzui deposit were mainly focused on: 1) the age and petrogenesis of the magmatic intrusions (Xie et al. 2011a; Duan and Jiang. 2017); 2) ore deposit geology, including mineralization and alteration paragenesis (Guo et al. 2007; Zhang 2015; Tian et al. 2019); 3) alteration mineralogy and its exploration implications (Tian et al. 2019), 4) ore mineralogy (Au-/Ag-bearing minerals, Zhang et al. 2016; quartz, Zhang et al. 2019), and 5) controlling factors of sulfide precipitation, notably (i) phase separation (fluid boiling), as supported by the coexisting vapor-, liquid-rich, and hypersaline fluid inclusions with similar homogenization temperatures (250–400 °C) in the main-ore stage, and the widespread occurrence of hydrothermal breccia (Zhang 2015); (ii) mixing of magmatic-hydrothermal and meteoric fluids in the late-ore stage, as supported by the wide H–O isotope composition range and the major fluid salinity drop from the main-ore to late-ore stage (Zhang 2015); (3) boiling-related neutralization of the acidic magmatic-hydrothermal fluids in the main-ore stage, revealed by the textural and trace element features of main-stage quartz (Zhang et al. 2019).

SAMPLES AND METHODS

Sampling

In this study, we conducted core logging for 13 drill holes shown on Fig. 2a, with a total length of 15566 m. A total of 1901 samples were collected from these 13 drill holes based on alteration and mineralization, and detailed petrographic descriptions were conducted on 398 polished sections. Accordingly, a total of 133 representative pyrite-bearing samples were selected, among which 35 and 98 samples were collected from the orebodies and mineralized wallrocks (including 62 hornfels, 10 dolomitic marble, and 26 quartz diorite), respectively. Detailed sampling locations are shown in Figure 2 (for samples from exploration line 28#) and listed in

Appendix I.

BSE imaging

Prior to the LA-ICP-MS in-situ trace elements analysis, BSE imaging of pyrite grains in Stages IV and V was performed with a Shimadzu EPMA-1720 Series (Japan) electron probe microanalyzer (EPMA) analysis in the School of Geosciences and Info-Physics of the Central South University. Working conditions of the BSE imaging include 15 kv (acc. voltage) and 2.0×10^{-8} A (probe current) (Zhang et al. 2017c).

LA-ICP-MS in-situ analysis of trace elements

Laser ablation analyses were carried out at the CODES LA-ICP-MS Laboratory, University of Tasmania. The analyses used a RESOlution laser platform equipped with a Coherent COMPex Pro 193 nm excimer laser and Lauren Technic S155 large format sample cell, coupled to an Agilent 7700 quadrupole ICP-MS. The laser operating parameters were optimized for pyrite analysis using a fluence of 2.7 J/cm^2 and 5 Hz laser repetition rate. Samples were ablated in an atmosphere of pure He flowing through the sample cell at a rate of 0.4 L/min, and immediately mixed with ~ 1 L/min Ar in the exit funnel before entering the ICP-MS. The ICP-MS instrument was optimized balancing sensitivity on mid- to high-mass and production of molecular oxide interferences (i.e., ^{232}Th^{16}O+/^{232}Th+) and doubly charged ion interferences (i.e., ^{140}Ce++/^{140}Ce+), with both interferences maintained at levels below 0.2%. Many element isotopes (^{23}Na, ^{24}Mg, ^{27}Al, ^{29}Si, ^{34}S, ^{39}K, ^{43}Ca, ^{49}Ti, ^{51}V, ^{53}Cr, ^{55}Mn, ^{59}Co, ^{60}Ni, ^{65}Cu, ^{66}Zn, ^{75}As, ^{77}Se, ^{90}Zr, ^{93}Nb, ^{95}Mo, ^{107}Ag, ^{111}Cd, ^{118}Sn, ^{121}Sb, ^{125}Te, ^{157}Gd, ^{178}Hf, ^{181}Ta, ^{182}W, ^{195}Pt, ^{197}Au, ^{205}Tl, ^{208}Pb, ^{209}Bi, ^{232}Th, and ^{238}U) were measured to unravel the trace element contents of pyrite and to identify possible mineral inclusions in pyrite. Concentrations for the following elements in pyrite are reported here: Co, Ni, Cu, Zn, As, Se, Mo, Ag, Te, Au, Pb and Bi. For each spot analysis, the background signal is recorded for 30 seconds, then the laser is turned on and the targeted mineral is ablated while the ICP-MS collects data for each element for ~60 seconds. During the spot analysis, the material analyzed is typically dominated by the targeted mineral. Element signals that show no changes, gradual smooth changes, or changes consistent with chemical zonation are interpreted to be chemically bound into the crystal lattice. In contrast, analysis through homogeneously distributed micro-/nano-inclusions may also show no or gradual signal changes, and are therefore indistinguishable from the 'true' solid solution signal. Both types of elemental occurrences are hereby referred to as refractory. Elements that have signals with discrete, sharp changes in the laser signal, and can sometimes reach level to dilute target major element signals, are interpreted as being hosted in mineral inclusions or in adjacent minerals. To calculate the mineral trace element concentrations, the average signal over the time interval of interest is calibrated against the in-house reference standard STDGL3, a sulfide-rich glass for primary calibration for quantifying siderophile and chalcophile elements (Belousov et al. 2015). Laser spot size is set to 29 μm for all pyrite samples and 51 μm for the STDGL3 standard glass. Larger spot size used on the standard glass provides higher precision to the analyses, and the slight increase in uncertainties (due to the spot size mismatch between standards and unknowns) is acceptable given the large dynamic range of the data in this study. Data reduction was performed with the Norris Scientific LADR software package.

RESULTS

Petrogenesis of pyrite

Pyrite at Jiguanzui is widely found in the main Cu-Au ore stage (stage IV: quartz–pyrite–chalcopyrite stage) and stage V calcite–sulfide mineralization (Fig. 3). Pyrite occurs as massive in orebodies, or as stockworks and clumps in the mineralized wallrocks of the Puqi Fm. hornfels, the Jialingjiang Fm. dolomitic marble and quartz diorite. Moreover, local post-ore pyrite in the late stage of Stage V can be also observed in the orebodies.

Pyrite in the main Cu-Au ore stage (Py1)

Py1 is characterized by the coexistence with quartz, and contains five types according to their mineral assemblages: (1) quartz–pyrite (Py1a), (2) quartz–calcite–pyrite (Py1b), (3) quartz–sericite–pyrite (Py1c), (4) quartz–chlorite ± epidote–pyrite (Py1d) and (5) quartz–K-feldspar–pyrite (Py1e).

Py1a is the most common and widespread pyrite type in the main ore stage, and primarily occurs as massive in the orebodies and veins in the wallrocks. Py1a in the orebodies is primarily anhedral and intergrown with quartz and chalcopyrite (Fig. 4a), and commonly replaces garnet (Fig. 4b) and magnetite (Fig. 4c), and trapped some hessite grains (Zhang et al. 2016). Py1a veins are widely distributed in the Puqi Fm. hornfels (Fig. 4d–h) and quartz diorite, and commonly occurs as straight veins (ca. 0.2 – 3.0 cm wide) with distinct wavy discoloration halo (Fig. 4f–g). Some miarolitic quartz cavities (Fig. 4d) are locally present in Py1a veins. Py1a in veins are commonly anhedral (Fig. 4b). Chalcopyrite and molybdenite coexist locally with Py1a in veins

(Fig. 4d–g). Moreover, the stage V calcite–pyrite veins commonly crosscut Py1a veins (Fig. 4f). The quartz/pyrite ratios vary in Py1a veins in the wallrocks, but are distinctly higher than those in the orebodies. Apart from occurring in veins, Py1a is also present as irregular clumps in the hornfels (Fig. 4h).

Py1b is also widely distributed in both the orebodies and as veins/clumps in the various types of wallrocks. Py1b in the orebodies commonly occurs as anhedral grains or massive aggregates coexisting with quartz, calcite, and chalcopyrite, together with trace bornite and chalcocite (Tian et al. 2019; Fig. 4i). Py1b in the wallrocks is commonly hosted in straight veins (mostly 0.2 – 2.0 cm wide; Fig. 4j) or irregular clumps (2 – 8 cm in size; Fig. 4k), in which Py1b primarily occurs as anhedral grain aggregates (Fig. 4i–l). Trace molybdenite was locally observed in Py1b veins, but Cu-bearing minerals are largely absent (Fig. 4j). More importantly, Py1b formed after Py1a, as indicated by the quartz–calcite–Py1b veins cut quartz–Py1a veins (Fig. 4l). Moreover, Py1b veins/clumps in wallrocks are also cut by calcite–Py2a veins (Fig. 4k).

Py1c is characterized by its coexistence with anhedral quartz and sericite (Fig. 4m–o), and is locally distributed in the Puqi Fm. hornfels (ca. –800 to –200 m elevation) close to the shallow quartz diorite. The quartz–sericite–pyrite (Py1c) assemblage occurs as irregular clumps (primarily 1 – 3 cm in size) rather than veins (Fig. 4m). The majority of Py1c occur as anhedral grains (Fig. 4n), but some occur locally as subhedral-euhedral cubic crystals (Fig. 4o). Locally, clumps of quartz–sericite–hematite–pyrite were found in hornfels (434.9 m depth in drill core KZK13), in which early hematite was replaced by quartz–Py1c–sericite (Fig. 4o).

Py1d is characterized by its intergrowth with anhedral quartz and chlorite (Fig. 4p and q) and locally epidote (Fig. 4r), and is primarily distributed in the Puqi Fm. hornfels in the form of straight veins (primarily 3 – 10 mm wide, locally down to ca. 0.2 mm; Fig. 4p and q) or irregular clumps (primarily 1 – 5 cm in size; Fig. 4r). This type of vein or clump commonly shows distinct discolored alteration halo (Fig. 4p). Locally, quartz is only developed along both sides of veins (Fig. 4q).

Py1e coexists with quartz and K-feldspar, and primarily occurs as veins (generally 0.3 – 0.5 cm wide; Fig. 4s–t) in quartz diorite and the Puqi Fm. hornfels. These veins in quartz diorite are commonly wavy with distinct K-feldspar alteration halos (Fig. 4s), whereas those in hornfels are largely straight with anhedral K-feldspar grains and weak K-feldspar alteration halo (Fig. 4t). Py1e commonly occurs as anhedral grains in veins (Fig. 4s–t), or locally as irregular granular clumps in the hornfels.

Pyrite in the calcite-sulfide stage (Py2)

Py2 is characterized by its coexistence with abundant calcite, and occurs primarily in two mineral assemblages: (1) calcite–pyrite (Py2a) and (2) calcite–K-feldspar–pyrite (Py2b).

Py2a is widespread as massive in both the orebodies and veins in the wallrocks (esp. hornfels and dolomitic marble) at Jiguanzui. In the orebodies, Py2a is commonly subhedral-euhedral (Fig. 5a) and coexists with calcite, sphalerite, and galena (Fig. 5b). In hornfels and dolomitic marble, Py2a coexists with calcite as veins (Fig. 5c–g; primarily 2 – 10 mm wide) or stockworks (Fig. 5h and i). The veins in hornfels are commonly straight (Fig. 5c–d) with local wavy discoloration selvage (Fig. 5d), while that in the dolomitic marble is commonly curvy with coexisting calcite (Fig. 5e). Py2a in veins is commonly subhedral to euhedral (Fig. 5f), and occurs locally as discontinuous short veins (Fig. 5g). Additionally, hornfels and dolomitic marble occur locally as breccias, which are cemented by calcite–Py2a stockworks (intruding hornfels), where Py2a is commonly distributed along the vein margin (Fig. 5h), or intergrown with calcite in dolomitic marble (Fig. 5i). Calcite–Py2a veins commonly cut veins of Py1a (Fig. 5f) and Py1d, and clumps of Py1b (Fig. 4k) and Py1c (Fig. 5j), but are cut by later calcite veins (Fig. 5k).

Py2b is locally distributed in the Puqi Fm. hornfels as calcite–K-feldspar–pyrite clumps (mostly 5 – 10 mm in size; Fig. 5l) or veins (mostly 2 – 10 mm wide; Fig. 5m). Py2b is mostly anhedral, and the coexisting K-feldspar is commonly distributed on the rims of the clumps (Fig. 5l). Given the lack of clear crosscutting relationship, the age sequence between Py2a and Py2b cannot be established.

Post-ore pyrite (Py3)

Py3 is characterized by (1) bird's-eye pyrite (Py3a) and (2) fingerprint-like pyrite (Py3b).

Py3a is locally found in the orebodies, and its hand-specimen shows clear porous texture (Fig. 5n). It is commonly ellipsoidal (50 – 500 μm in size) or with irregular bird's-eye texture and replaced the porous massive Py1b along fractures (Fig. 5o).

Py3b is also locally found in the orebodies, and occurs as pseudomorphs of Py3a (ca. 50 – 500 μm in size; Fig. 5p), and remnants of Py3a is locally preserved in Py3b (Fig. 5p). Due to the recrystallization of Py3a into Py3b, the consequent volume reduction may have formed the fissures observed, which are now filled by later calcite (Fig. 5p).

Pyrite textures

In this study, based on the distribution of the different pyrite types, 37 samples (Py1a = 23, Py1b = 2, Py1c = 2, Py1d = 4, Py1e = 2, Py2a = 3, and Py2b = 1) were selected for BSE imaging. Py1a grains commonly show homogeneous internal texture, with no zoning or replacement features (Fig. 6a and b). Additionally, some telluride (Fig. 6a) and bismuthide (Fig. 6b) occur as mineral inclusions in Py1a grains. Similar to Py1a, grains of Py1b (Fig. 6c), Py1c (Fig. 6d), Py1d (Fig. 6e), Py1e (Fig. 6f), Py2a (Fig. 6g) and Py2b (Fig. 6h) also show homogenous internal texture. Meanwhile, Py1c and Py1d grains are commonly quartz inclusion-bearing (Fig. 6d) and fractured (Fig. 6e). It is common that Py2a grains have some sphalerite inclusions, consistent with the well-developed sphalerite mineralization in the calcite-sulfide stage (Tian et al. 2019). A light-color zone is locally observed in Py1c grains (Fig. 6i). Additionally, the local offsetting (Fig. 7a) and synchronous (Fig. 7b) LA-ICP-MS time-resolved signals between Co and Ni also indicate alternating Co-Ni zoning in Py1a grains.

Pyrite trace element compositions

A total of 868 LA-ICP-MS spot analyses were completed on the Jiguanzui pyrite, among which 177 and 438 spots are on Py1a from the orebodies and the wallrocks, respectively. A total of 52 data were discarded because of obvious signal disturbance resulted from the other mineral phases or mineral inclusions. Trace elements contents of the Jiguanzui pyrite are listed in Appendix I, summarized in Table 1, and shown in Figure 8.

In general, Py1 has higher Co, Ni, Se, Ag, and W, and lower V, Zn, As and Mo contents than Py2. Although Py1 has generally similar Cu-Au contents to Py2, in the orebodies Py1 (Cu: 1.33

ppm; Au: 0.027 ppm) has higher median Cu-Au contents than Py2 (median Cu: 1.12 ppm; Au: 0.011 ppm (Table 1), consistent with that Py1 was formed in the main ore stage. As the most common pyrite type in the main ore stage, Py1a in the orebodies has higher As-Ag-Te but lower Co-Ni-Se contents than Py1a from veins/clumps in the wallrocks. Py2a contains high Zn-Mo contents, consistent with the sphalerite and molybdenite mineralization in the Stage V. Py3a and Py3b have commonly higher trace element contents, especially Cu, Zn, As, Mo, Ag, Au, and Pb (Fig. 8).

DISCUSSION

Controls on trace element distributions in the Jiguanzui pyrite

Previous studies revealed significant trace element concentrations of Au, Ag, Cu, Pb, Zn, Co, Ni, As, Sb, Se, Te, Tl and Bi in pyrite (Reich and Becker 2006; Large et al. 2007, 2009; Deditius et al. 2011; Reich et al. 2013). These trace elements in pyrite may occur in three forms: (1) as solid solution within the crystal lattice; (2) homogeneously in nano-sized mineral (silicate/carbonate minerals or other sulfides) inclusions; (3) in micron-sized inclusions (Thomas et al. 2011; Ciobanu et al. 2012; Belousov et al. 2016). LA-ICP-MS time-resolved signal spectra can provide useful information on the trace element occurrence in pyrite (Belousov et al. 2016). The time-resolved signal spectra of Co, Ni, Se, Te, and As for most Jiguanzui pyrite samples are flat and stable (Fig. 7c and d), indicating homogeneous distributions of these elements. Nickel and Co are readily incorporated into the pyrite lattice via the replacement of Fe, and are not readily released during hydrothermal pyrite recrystallization, while Se and Te enter the lattice by replacing sulfur

(Huerta-Diaz and Morse 1992; Morse and Luther 1999; Tribovillard et al. 2006; Large et al. 2009; Koglin et al. 2010). Meanwhile, As commonly substitutes the tetrahedrally-coordinated S^- or octahedrally-coordinated Fe^{2+} as As^- or $As^{2+/3+}$, respectively (Fleet and Mumin 1997; Savage et al. 2000; Deditius et al. 2008; Keith et al. 2018). Therefore, the elements of Co, Ni, Se, Te and As most likely occur as solid solution in the Jiguanzui pyrite, although they can also occur in homogenously-distributed nano-inclusions (Gregory et al. 2015; Li et al. 2020). The occurrence of micron-scaled mineral inclusions are reflected by local signal peaks of Te (Fig. 7e), probably formed by telluride-bearing mineral inclusions (Fig. 6a).

Lead cannot enter the pyrite crystal lattice due to its large ionic size, and precipitates more readily than Fe from an aqueous fluid as metal sulfide, leading to the common presence of Pb-bearing mineral inclusions in pyrites (Huerta-Diaz and Morse 1992; Morse and Luther 1999; Koglin et al. 2010). The presence of Pb–Bi-bearing mineral inclusions is indicated by the spectral peaks of Pb–Bi–Te–Ag–Sb (Fig. 7e), Pb–Bi–Cu–Co, and Pb–Bi (Fig. 7f). Importantly, the local flat and stable Pb-Bi signal spectra (Fig. 7f) can infer the homogeneous distribution of Pb–Bi nano-inclusions in pyrite, rather than solid solution in the pyrite crystal lattice.

Gold and As concentrations of hydrothermal pyrites can constrain the saturation state of Au-bearing fluids from which the As-bearing pyrite precipitated, and provide information on Au distribution in pyrite (Reich et al. 2005). For the Jiguanzui pyrite, Au and As concentrations dominantly plot below the Au solubility curve (Fig. 9a), indicating that the Au occurs primarily as Au^{+1} (solid solution) in pyrite. However, the few data points fall above the solubility line suggest the existence of local Au nanoparticles in pyrite, consistent with the microscopic observation

DOI: https://doi.org/10.2138/am-2022-8118. http://www.minsocam.org/

reported by Zhang et al. (2016). The high level of outliers for Zn and Mo in Py1a, the wide Zn-Mo concentration ranges of Py2a, and the high Mo-Zn contents of Py3 (Fig. 8) all suggest that Zn and Mo occur as micro-inclusions. Meanwhile, the high Cu-W contents of Py3 also reveal their micro-inclusions occurrence (Fig. 8).

Origin of the Jiguanzui pyrite

Physicochemical conditions for pyrite formation have major impact on the pyrite Co-Ni contents and Co/Ni ratios, suggesting that Co/Ni ratios can be indicative for the pyrite origin (Loftus-Hills and Solomon 1967; Bralia et al. 1979; Craig et al. 1998; Clark et al. 2004). Most Jiguanzui pyrite samples have Co/Ni = 0.1 to 10 (Fig. 9b), resembling pyrite (Co/Ni = 1–10) from magmatic-hydrothermal deposits (Reich et al. 2016). Diagenetic pyrite has commonly Co/Ni ≤ 2, whereas hydrothermal pyrite has commonly higher Co/Ni values (Large et al. 2009, 2014; Gregory et al. 2015). Significant proportion of the Jiguanzui pyrite samples have their Co/Ni ratios ⩾ 2 (Py1a = 42.15%, Py1b = 35.29%, Py1d = 77.14%, Py1e = 28.26%, Py2a = 35.00%, and Py2b = 44.44%), demonstrating their hydrothermal origin, which is also supported by their coexistence with hydrothermal minerals (quartz, calcite, K-feldspar, chlorite, epidote). Their varying Co/Ni ratios (Appendix I) are likely associated with some Co-bearing mineral inclusions, as revealed by the spectral peaks of Pb–Bi–Cu–Co (Fig. 7f). This also suggests changes in fluid compositions and/or physicochemical conditions (Real et al. 2020), consistent with the interpreted phase separation (fluid boiling) in the main-ore stage and the hydrothermal-meteoric fluid mixing in the late-ore stage (Zhang 2015). Py1c has relatively narrow Co/Ni ratios (0.07 to 1.94, median

0.82), suggesting that Py1c may have had a major sedimentary source. The Cu/Ni (0.0002–0.084), Zn/Ni (0.0005–0.024) and As/Ni (0.011–0.346) ratios of Py1c draw the similar conclusion, as previous studies suggested sedimentary pyrite has 0.01 < Cu/Ni < 10, 0.01 < Zn/Ni < 10, and 0.1 < As/Ni < 10 (Gregory et al. 2015, 2017). However, this does not rule out potential hydrothermal contribution owing to the coexistence with hydrothermal quartz and sericite. The fact that Py1c occurs only as irregular clumps in the Puqi Fm. hornfels suggests possible intensive fluid-rock interactions, which may have been responsible for the low Co/Ni ratios of Py1c (Real et al. 2020). Moreover, sulfur isotope analysis for the Jiguanzui pyrite ($\delta^{34}S$ = 1.30–4.50‰; Zhang 2015) further reveals probable genetic links with magmatic-hydrothermal fluids. The Co/Ni (0.97–7.30, mostly > 2), Cu/Ni (8.94–186) and As/Ni (0.80–11.7) ratios of Py3a rule out a sedimentation origin, although its Zn/Ni ratios (0.02–2.20) resemble typical sedimentary pyrite. Meanwhile, the obviously high trace element contents (Fig. 8) of Py3a occurring as aggregates of microcrystalline pyrite (Sun et al. 2019) suggest its rapid growth, which could facilitate the incorporation of trace elements through adsorption onto the pyrite surface (Abraitis et al. 2004). The ore-forming fluids may have shifted from being dominantly magmatic-hydrothermal in the main ore stage to meteoric in the late stage (Zhang 2015), causing significant physicochemical fluctuations in the fluids. The waning of the magmatic-hydrothermal system and the increasing meteoric water influx in the post-ore stage may have led to the probable rapid growth of Py3.

Trace element temporal variations and implications on ore-forming fluid evolution

Previous studies revealed that pyrite chemistry can unravel hydrothermal ore-forming processes (Large et al. 2009; Reich et al. 2013; Deditius et al. 2014), considering that trace element incorporation into pyrite is dependent on changes in physicochemical fluid parameters, including temperature, pH, fO_2, and fluid compositions. Such changes can be achieved by processes such as fluid mixing, boiling, oxidation, acidification, and/or hydrothermal fluid replenishment (Kouzmanov et al. 2010; Deditius et al. 2014; Revan et al. 2014; Wu et al. 2018).

Given that magmatic fluids have commonly higher Se concentrations than meteoric water (Huston et al. 1995; Rowins et al. 1997, Fitzpatrick 2008; Li et al. 2018b), the much higher (one order of magnitude) Se content of Py1 (median 50.5 ppm) than Py2 (median 13.6 ppm) is consistent with the magmatic-hydrothermal to meteoric shift from the main ore stage to the late stage fluids. This is also supported by the H–O isotope variation and the abrupt salinity drop in fluid inclusions from these stages (Zhang 2015; Fig. 10). Therefore, the meteoric water influx into the ore-forming fluids is an important factor for the decreasing Se contents from Py1 to Py2. Moreover, more Se can be hosted by galena than by chalcopyrite, although they both can host more Se than pyrite (Wohlgemuth-Ueberwasser et al. 2015; Williams et al. 2015), which may be another reason for the decreasing Se contents from Py1 (coexisting with chalcopyrite) to Py2 (coexisting with galena) (Fig. 3). Although previous studies revealed that Se concentration in hydrothermal pyrite correlates negatively with fluid temperature (Huston et al. 1995; Keith et al. 2018), the apparent decrease of Se concentrations from Py1 to Py2 is not consistent with the fluid inclusion microthermometry data (avg. 331 °C for Stage IV; avg. 173 °C for Stage V; Zhang 2015), likely because this cooling is resulted from the mixing of meteoric water. Therefore, temperature variations may have less effect on the Se variations than by fluid source and coexisting minerals. Cobalt and Ni are typical mantle-derived elements, and magmatic-hydrothermal fluids have commonly higher Co-Ni contents than meteoric water (Loftus-Hills and Solomon 1967; Bralia et al. 1979; Chen et al. 1987). Similarly, meteoric water contribution in the calcite-sulfide stage may have been an important factor for the decrease of Co (Py1: median 38.7 ppm; Py2: median 4.10 ppm) and Ni (Py1: median 30.1 ppm; Py2: median 13.4 ppm), consistent with the broadly positive Co vs. Ni correlation in the Jiguanzui pyrite (Fig. 9b). Meanwhile, the chalcophile and siderophile properties of Co and Ni (Dehaine et al. 2021) may have caused their obvious decrease in the ore-forming fluids after the precipitation of abundant main-stage pyrite and chalcopyrite, again causing the decreasing Co-Ni concentrations from Py1 to Py2.

Gradual enrichment of pyrite trace elements (esp. As) that replace S^{2-} under reducing conditions was suggested (Reich et al. 2005; Ward et al. 2017). Fluid temperature decrease would probably also result in As enrichment in pyrite (Li et al. 2018a), consistent with increasing As concentrations from Py1 (median 9.45 ppm) to Py2 (median 138 ppm) and the general temperature drop from Stage IV to V (Zhang 2015). The Zn enrichment in Py2 is likely caused by pH increase, resulting from the reaction with carbonate rocks. This is because pH increase is the most efficient mechanism for Zn precipitation at both high and low temperatures (Kouzmanov and Pokrovski 2012). Although Mo solubility increases with increasing pH, MoS_2 has extremely low solubility at low temperatures (Kouzmanov and Pokrovski 2012). Therefore, cooling is likely the main factor for Mo enrichment in Py2.

Spatial variation of pyrite trace element contents and its skarn metallogenic implications

In the skarn mineralization, abundant CO_2 is released into the ore fluids during the conversion of carbonate to skarn, which increases the mineral system pressure (Meinert et al. 2005; Fig. 10a). When fluid pressure exceeds the lithostatic load, shear stress accumulation may have caused extensive hydraulic fracturing (Sibson et al. 1988) and sudden fluid pressure drop, coupled with fluid boiling and phase separation (Fig. 10b), as supported by the coexisting vapor-, liquid-rich, and hypersaline fluid inclusions in Stage IV quartz from the Jiguanzui orebodies (Zhang 2015). This fluid boiling (phase separation) is inferred to be an important factor controlling the main metal sulfide precipitation to form orebodies at Jiguanzui (Zhang 2015). The subsequent sealing of the hydraulic fractures owing to the fluid condensation may have formed the veins/clumps in the mineralized wallrocks (esp. hornfels; Fig. 10c). At the low-to-moderate temperatures (≤ 350°C), the main effect of fluid boiling and phase separation is likely the segregation of acidic volatiles (CO_2, HCl, H_2S, and SO_2) from the liquid phase, resulting in the pH increase of the ore fluids (Ohmoto 1972; Drummond and Ohmoto 1985). In contrast, in high-temperature (>400°C) high-salinity fluids, the pH change of the liquid phase led by the acidic volatile removal is likely compensated by rapid fluid equilibration with silicate rocks and an increase in fluid salinity, both favoring sulfide dissolution (Kouzmanov and Pokrovski 2012). Given that the coexisting vapor-, liquid-rich, and hypersaline fluid inclusions in the main-ore stage have similar homogenization temperatures (250 – 400 ℃) (Zhang 2015), the fluid pH rise (resulting from acidic volatile segregation) may have caused Py1a precipitation in the orebodies. This agrees with the acidic magmatic fluid neutralization led by fluid boiling, as supported by the trace element compositions of Stage IV quartz (Zhang et al. 2019). Given that Stage IV Py1a is widely distributed at Jiguanzui, it can serve as an indicator mineral to document pyrite trace element spatial variations in the skarn system. Our LA-ICP-MS results reveal that Py1a in the orebodies has higher As (median 58.2 ppm), Ag (median 0.207 ppm) and Te (median 6.82 ppm), and lower Co (median 14.1 ppm), Ni (median 10.5 ppm) and Se (median 37.9 ppm) than those in veins/clumps in the wallrocks (median As = 7.05 ppm, Ag = 0.101 ppm, Te = 1.04 ppm, Co = 49.6 ppm, Ni = 34.1 ppm, and Se = 60.8 ppm) (Table 1).

Fluid boiling and phase separation has strong impact on fluid chemistry (Román et al. 2019). Boiling and phase separation may lead to precipitation of Ag because Ag has lower solubility with pH increasing (Spycher and Reed 1989; Simmons and Browne 2000; Kouzmanov and Pokrovski 2012). Tellurium shows strong affinity to the vapor phase (Cooke and McPhail 2001; Pudack et al. 2009), but such affinity decreases markedly during fluid boiling under more oxidizing conditions (Grundler et al. 2013). Under these conditions, minor Te would still be partitioned into the vapor phase, but most Te would be concentrated with Au in the liquid phase, leading to the coupled Au-Te enrichments (Keith et al. 2020). This conforms to higher concentrations of Te in Py1a from the orebodies. In addition, the higher Ag-Te enrichments in Py1a from the orebodies than those in

DOI: https://doi.org/10.2138/am-2022-8118. http://www.minsocam.org/

the wallrocks is consistent with the occurrence of hessite in the former (Zhang et al. 2016). The elevated pH by phase separation would increase the As solubility in the fluids, and most As would be concentrated in the liquid phase at depth (Pokrovski et al. 2013). Furthermore, As is ubiquitous in porphyry-skarn systems and is commonly associated with Au–Cu mineralization (orebody) in the form of soluble hydroxide species (Kouzmanov and Pokrovski 2012). These may have given rise to higher As concentrations of Py1a in the orebodies than that in the wallrocks.

Given that the Se content in hydrothermal pyrite is controlled by fluid temperature (Huston et al. 1995; Keith et al. 2018), cooling during fluid ascent along fractures would favor Se enrichment in Py1a veins/clumps in the wallrocks. Previous studies revealed that cooling may destabilize Co-chloride complexes in hydrothermal fluids, and a temperature drop from 300 to 200 °C could cause an up to two orders of magnitude drop in the Co content (Migdisov et al. 2011). Therefore, fluid cooling may have promoted Co precipitation and increased the Py1a Co content in the wallrocks. Given the similar geochemical behaviors between Co and Ni, this process may have also increased the Py1a Ni content in the wallrocks (Loftus-Hills and Solomon 1967; Bralia et al. 1979).

Veins associated with hydraulic fracturing in the wallrocks could facilitate proximal alteration in the skarn system (Meinert et al. 2005). Therefore, the trace element spatial variations of Py1a could serve as a vector toward the hydrothermal (possibly also mineralization) center. Py1a in the orebodies has distinctly higher As, and lower Se, Co and Ni contents than Py1a in the wallrocks (Table 1), and their concentration contour diagrams in the Jiguanzui 28# exploration profile also show clear coupling relations between the majority of the orebodies along/near the intrusive contact and Py1a with high As and low Se, Co and Ni contents (Fig. 11). Therefore, we infer that Py1a with high As and low Se, Co and Ni contents could serve as an exploration pathfinder for the Jiguanzui skarn orebodies hosted in the intrusive contact. Meanwhile, Py1a in the wallrocks is genetically associated with extensive hydraulic fracturing, coupled with fluid boiling, phase separation, and pH and fO_2 increase. Fluid boiling and pH increase were inferred as important factors for metal sulfide precipitation in the main ore stage (Zhang 2015; Zhang et al. 2019; Fig. 11b). Furthermore, hydraulic fracturing of the wallrocks likely provided fluid conduits for meteoric water influx, and promoted fluid mixing between meteoric water and magmatic-hydrothermal fluids (Fig. 10d), which is responsible for the decreasing Se-Co-Ni concentrations from Py1 to Py2, and may have led to Stage V sulfide mineralization (Zhang 2015). Therefore, the veins and clumps in wallrocks likely had a pivotal contribution to the skarn mineralization.

IMPLICATIONS

At Jiguanzui, meteoric water input, temperature drop, pH increase resulting from reaction with carbonate rocks, and the formation of abundant Stage V galena likely caused the Se-Co-Ni depletions and As-Zn-Mo enrichments from Py1 to Py2. Decompression and phase separation (fluid boiling) resulted from extensive hydraulic fracturing and the coupled higher temperature, pH and fO_2 for Py1a in orebodies than for those in wallrocks predominantly led to its Se-Co-Ni depletions and As-Ag-Te enrichments. More importantly, this study highlights the significance of wallrock hydraulic fracturing, fluid-rock reaction, and the fluid physicochemical evolution in the skarn ore-forming process, and suggest the potential use of pyrite trace element geochemistry for exploring Au–Cu skarn mineral systems.

ACKNOWLEDGEMENTS

We especially thank Prof. Ross R. Large and Dr. Daniel Gregory for their insightful suggestions for an earlier version of the manuscript. Our especial thank also goes to the staffs from Team 1 of Hubei Geological Bureau for their field assistance, and to Dr. Chao Wu for helping with the LA-ICP-MS trace elements analysis.

FUNDING

This research was financially supported by the National Natural Science Foundation of China (41702065, 41725009).

References

Abraitis, P.K., Pattrick, R.A.D., Vaughan, D.J. (2004) Variations in the compositional, textural, and electrical properties of natural pyrite: A review. International Journal of Mineral Processing, 74, 41–59.

Belousov, I., Danyushevsky, L., Olin, P., Gilbert, S., Thompson, J. (2015) STDGL3 – A new calibration standard for sulphide analysis via LA-ICP-MS. Goldschmidt 2015 Abstracts, 251.

Belousov, I., Large, R.R., Meffre, S., Danyushevsky, L.V., Steadman, J., Beardsmore, T. (2016) Pyrite compositions from VHMS and orogenic Au deposits in the Yilgarn Craton, Western Australia: Implications for gold and copper exploration. Ore Geology Reviews, 79, 474–499.

Bralia, A., Sabatini, G., Troja, F. (1979) A revaluation of the Co/Ni ratio in pyrite as geochemical tool in ore genesis problems. Mineralium Deposita, 14, 353–374.

Chen, G.Y., Sun, D.S., Yin, H.A. (1987) Genetic Mineralogy and Mineral Mineralogy. Chongqing Publishing Group, pp. 35–41 (in Chinese).

Ciobanu, C.L., Cook, N.J., Utsunomiya, S., Kogagwa, M., Green, L., Gilbert, S., Wade, B. (2012) Gold-telluride nanoparticles revealed in arsenic-free pyrite. American Mineralogist, 97, 1515–1518.

Clark, C., Grguric, B., Mumm, A.S. (2004) Genetic implications of pyrite chemistry from the Paleoproterozoic Olary Domain and overlying Neoproterozoic Adelaidean sequences, northeastern South Australia. Ore Geology Reviews, 25, 237–257.

Cooke, D.R., McPhail, D.C. (2001) Epithermal Au-Ag-Te mineralization, Acupan, Baguio district, Philippines: Numerical simulations of mineral deposition. Economic Geology, 96, 109–131.

Cooke, D.R., Ciobanu, C.L., Meria, D., Silcock, D., Wade, B. (2013) Arsenopyrite-pyrite association in an orogenic gold ore: Tracing mineralization history from textures and trace elements. Economic Geology, 108, 1273–1283.

Craig, J.R., Vokes, F.M., Solberg, T.N. (1998) Pyrite: Physical and chemical textures. Mineralium Deposita, 34, 82–101.

Cromie, P., Makoundi, C., Zaw, K., Cooke, D.R., White, N., Ryan, C. (2018) Geochemistry of Au-bearing pyrite from the Sepon Mineral District, Laos DPR, Southeast Asia: Implications for ore genesis. Journal of Asian Earth Sciences, 164, 194–218.

Deditius, A.P., Reich, M., Kesler, S.E., Utsunomiya, S., Chryssoulis, S.L., Walshe, J., Ewing, R.C. (2014) The coupled geochemistry of Au and As in pyrite from hydrothermal ore deposits. Geochimica et Cosmochimica Acta, 140, 644–670.

Deditius, A.P., Utsunomiya, S., Renock, D., Ewing, R.C., Ramana, C.V., Becker, U., Kesler, S.E. (2008) A proposed new type of arsenian pyrite: composition, nanostructure and geological significance. Geochimica et Cosmochimica Acta, 72, 2919–2933.

Deditius, A., Utsunomiya, S., Reich, M., Kesler, S.E., Ewing, R.C., Hough, R., Walshe, J. (2011) Trace metal nanoparticles in pyrite. Ore Geology Reviews, 42, 32–46.

Dehaine, Q., Tijsseling, L.T., Glass, H.J., Törmänen, T. (2021) Geometallurgy of cobalt ores: A review. Minerals Engineering, 160, 106656.

Drummond, S.E., Ohmoto, H. (1985) Chemical evolution and mineral deposition in boiling hydrothermal systems. Economic Geology, 80, 126–147

Duan, D.F., Jiang, S.Y. (2017) The composition of pyroxene and amphibole in ore-related pluton in Jiguanzui Au-Cu skarn deposit, Edong region: Implication for the magma evolution and mineralization. Acta Petrological Sinica, 33(11), 3507–3517.

Feng, Y.Z., Zhang, Y., Xie, Y.L., Shao, Y.J., Lai, C. (2020) Pyrite geochemistry and metallogenic implications of Gutaishan Au deposit in Jiangnan Orogen, South China. Ore Geology Reviews, 117, 103298.

Fleet, M.E., Chryssoulis, S.L., Maclean, P.J., Davidson, R., Weisener, C.G. (1993) Arsenian pyrite from gold deposits: Au and As distribution investigated by SIMS and EMP, and color staining and surface oxidation by XPS and LIMS. Canadian Mineralogist, 31, 1–17.

Fleet, M.E., and Mumin, H. (1997) Gold-bearing arsenian pyrite and marcasite and arsenopyrite from Carling

Trend gold deposits and laboratory synthesis. American Mineralogist, 82, 182–193.

Fitzpatrick, A.J. (2008) The measurement of the Se/S ratios in sulfide minerals and their application to ore deposit studies. Queen's University, Kingston, Canada, 203 p.

Franchini, M., McFarlane, C., Maydagan, L., Reich, M., Lentz, D.R., Meinert, L., Bouhier, V. (2015) Trace metals in pyrite and marcasite from the Agua Rica porphyry-high sulfidation epithermal deposit, Catamarca, Argentina: Textural features and metal zoning at the porphyry to epithermal transition. Ore Geology Reviews, 66, 366–387.

Gregory, D.D., Large, R.R., Halpin, J.A., Baturina, E.L., Lyons, T.W., Wu, S., Danyushevsky, L., Sack, P.J., Chappaz, A., Maslennikov, V.V., Bull, S.W. (2015) Trace Element Content of Sedimentary Pyrite in Black Shales. Economic Geology, 110(6), 1389–1410.

Gregory, D.D., Large, R.R., Bath, A.B., Steadman, J.A., Wu, S., Danyushevsky, L., Bull, S.W., Holden, P., Ireland, T.R. (2016) Trace element content of pyrite from the Kapai Slate, St. Ives gold district, Western Australia. Economic Geology, 111(6), 1297–1320.

Gregory, D.D., Lyons, T.W., Large, R.R., Jiang, G., Stepanov, A.S., Diamond, C.W., Figueroa, M.C., Olin, P. (2017) Whole rock and discrete pyrite geochemistry as complementary tracers of ancient ocean chemistry: An example from the Neoproterozoic Doushantuo Formation, China. Geochimica et Cosmochimica Acta, 216, 201–220.

Grundler, P.V., Brugger, J., Etschmann, B.E., Helm, L., Liu, W.H., Spry, P.G., Tian, Y., Testemale, D., Pring, A. (2013) Speciation of aqueous tellurium(IV) in hydrothermal solutions and vapors, and the role of oxidized tellurium species in Te transport and gold deposition. Geochimica et Cosmochimica Acta, 120, 298–325.

Guo, C.Z., Wei, Q.M., Ye, H. (2007) Occurrence of cryptoexplosive breccia and porphyry type orebodies in

Jiguanzui deposit and their Characteristics. Metal Mine, 368, 52–55 (in Chinese with English abstract).

Heinrich, C.A. (2005) The physical and chemical evolution of low-salinity magmatic fluids at the porphyry to epithermal transition: A thermodynamic study. Mineralium Deposita, 39, 864–889.

Heinrich, C.A., Driesner, T., Stefánsson, A., Seward, T.M. (2004) Magmatic vapor contraction and the transport of gold from porphyry to epithermal ore deposits. Geology, 39, 761–764.

Huston, D.L., Sie, S.H., Suter, G.F., Cooke, D.R., Both, R.A. (1995) Trace elements in sulfide minerals from eastern Australian volcanic-hosted massive sulfide deposits. 1. Proton microprobe analyses of pyrite, chalcopyrite, and sphalerite, and. 2. Selenium levels in pyrite – comparison with delta-S-34 values and implications for the source of sulfur in volcanogenic hydrothermal systems. Economic Geology, 90, 1167–1196.

Huerta-Diaz, M.A., Morse, J.W. (1992) Pyritization of trace metals in anoxic marine sediments. Geochimica et Cosmochimica Acta, 56, 2681–2702.

Ke, Y.F., Cai, H.G., Du, K., Wu, Y.X., Yuan, H.W. (2016) Analyses of Geological Characteristics and Prospecting Potential of Jiguanzui Cu–Au Deposits in Daye City, Hubei Province. Resources Environment and Engineering, 30, 817–824 (in Chinese with English abstract).

Keith, M., Häckel, F., Haase, K.M., Schwarz-Schampera, U., Klemd, R. (2016) Trace element systematics of pyrite from submarine hydrothermal vents. Ore Geology Reviews, 72, 728–745.

Keith, M., Smith, D.J., Jenkin, G.R.T., Holwell, D.A., Dye, M.D. (2018) A review of Te and Se systematics in hydrothermal pyrite from precious metal deposits: Insights into ore-forming processes. Ore Geology Reviews, 96, 269–282.

Keith, M., Smith, D.J., Doyle, K., Holwell, D.A., Jenkin, G.R.T., Barry, T.L., Becker, J., Rampe, J. (2020), Pyrite chemistry: A new window into Au-Te ore-forming processes in alkaline epithermal districts, Cripple Creek, Colorado. Geochimica et Cosmochimica Acta, 274, 172–191.

Koglin, N., Frimmel, H.E., Minter, W.E.L., Brätz, H. (2010) Trace element characteristics of different pyrite types in Mesoarchaean to Paleoproterozoic placer deposits. Mineralium Deposita, 45, 259–280.

Kouzmanov, K., Pettke, T., Heinrich, C.A. (2010) Direct analysis of ore-precipitating fluids: Combined IR microscopy and LA-ICP-MS study of fluid inclusions in opaque ore minerals. Economic Geology, 105, 351–373.

Kouzmanov, K., Pokrovski, G.S. (2012) Hydrothermal controls on metal distribution in porphyry Cu (-Mo-Au) systems. Society of Economic Geologists, Special Publication, 16, 573–618.

Large, R.R., Maslennikov, V.V., Robert, F., Danyushevsky, L.V., Scott, R.J., Chang, Z. (2007) Multi-stage sedimentary and metamorphic origin of pyrite and gold in the giant Sukhoi Log deposit, Lena Goldfield, Russia. Economic Geology, 102, 1233–1267.

Large, R.R., Danyushevsky, L., Hollit, C., Maslennikov, V., Meffre, S., Gilbert, S. (2009) Gold and trace element zonation in pyrite using a laser imaging technique: implications for the timing of gold in orogenic and Carlin-style sediment-hosted deposits. Economic Geology, 5, 635–668.

Large, R.R., Halpin, J.A., Danyushevsky, L.V., Maslennikov, V.V., Bull, S.W., Long, J.A., Gregory, D.D., Lounejeva, E., Lyons, T.W., Sack, P.J., McGoldrick, P.J., Calver, C.R. (2014) Trace element content of sedimentary pyrite as a new proxy for deep-time ocean–atmosphere evolution. Earth and Planetary Science Letters, 389, 209–220.

Li, J.W., Zhao, X.F., Zhou, M.F., Ma, C.Q., Zorano, S.S., Paulo, V. (2009) Late Mesozoic magmatism from the Daye region, eastern China: U–Pb ages, petrogenesis, and geodynamic implications. Contributions to

Mineralogy and Petrology, 157, 383–412.

Li, J.X., Hu, R.Z., Zhao, C.H., Zhu, J.J., Huang, Y., Gao, W., Li, J.W., Zhuo, Y.Z. (2019) Sulfur isotope and trace element compositions of pyrite determined by NanoSIMS and LA-ICP-MS: new constraints on the genesis of the Shuiyindong Carlin-like gold deposit in SW China. Mineralium Deposita, https://doi.org/10.1007/s00126-019-00929-w.

Li, X.H., Li, W.X., Wang, X.C., Qiu, L.L., Liu, L., Tang, Q.Q., Gao, Y.Y., Wu, F.Y. (2010) SIMS U–Pb zircon geochronology of porphyry Cu–Au–(Mo) deposits in the Yangtze River Metallogenic Belt, eastern China: Magmatic response to early Cretaceous lithospheric extension. Lithos, 119, 427–440.

Li, X.H., Fan, H.R., Yang, K.F., Hollings, P., Liu, X., Hu, F.F., Cai, Y.C. (2018a) Pyrite textures and compositions from the Zhuangzi Au deposit, southeastern North China Craton: implication for ore-forming processes. Contributions to Mineralogy and Petrology, 173, 73.

Li, R.C., Chen, H.Y., Xia, X.P., Yang, Q., Danyushevsky, L.V., Lai, C. (2018b) Using integrated in-situ sulfide trace element geochemistry and sulfur isotopes to trace ore-forming fluids: Example from the Mina Justa IOCG deposit (southern Perú). Ore Geology Reviews, 101, 165–179.

Li, Y., Selby, D., Li, X.H., Ottley, C.J. (2018) Multisourced metals enriched by magmatic-hydrothermal fluids in stratabound deposits of the Middle–Lower Yangtze River metallogenic belt, China. Geology, 46, 391–394.

Li, Z.L., Ye, L., Hu, Y.S., Chen, W., Huang, Z.L., Yang, Y.L., Danyushevsky, L. (2020) Trace elements in sulfides from the Maozu Pb-Zn deposit, Yunnan Province, China: Implications for trace element incorporation mechanisms and ore genesis. American Mineralogist, https://doi.org/10.2138/am-2020-6950.

Loftus-Hills, G., Solomon, M. (1967) Cobalt, nickel and selenium in sulfides as indicators of ore genesis. Mineralium Deposita, 2, 228–242.

Meinert, L.D. (1992) Skarns and skarn deposits. Geoscience Canada, 19, 145–162.

Meinert, L.D., Dipple, G.M., Nicolescu, S. (2005) World Skarn Deposits. In *Economic Geology 100th Anniversary Volume* 1905–2005, Elsevier: Amsterdam, The Netherlands, 299–336 p.

Migdisov, A.A., Zezin, D., Williams-Jones, A.E. (2011) An experimental study of cobalt (II) complexation in Cl^- and H_2S-bearing hydrothermal solutions. Geochimica et Cosmochimica Acta, 75, 4065–4079.

Morse, J.W., Luther, G.W. (1999) Chemical influences on trace metal-sulfide interactions in anoxic sediments. Geochimica et Cosmochimica Acta, 63, 3373–3378.

Ohmoto, H. (1972) Systematics of sulfur and carbon isotopes in hydrothermal ore deposits. Economic Geology, 67, 551–578.

Pan, Y.M., Dong, P. (1999) The Lower Changjiang (Yangzi/Yangtze River) metallogenic belt, east central China: intrusion- and wallrock-hosted Cu–Fe–Au, Mo, Zn, Pb, Ag deposits. Ore Geology Reviews, 15, 177–242.

Pokrovski, G.S., Borisova, A.Y., Bychkov, A.Y. (2013) Speciation and transport of metals and metalloids in geological vapors. Reviews in Mineralogy and Geochemistry, 76, 165–218.

Pudack, C., Halter, W.E., Heinrich, C.A., Petke, T. (2009) Evolution of magmatic vapor to gold-rich epithermal liquid: The porphyry to epithermal transition at Nevados de Famatina, Northwest Argentina. Economic Geology, 104, 449–477.

Real, I., Thompson, J.F.H., Simon, A.C., Reich, M. (2020) Geochemical and isotopic signature of pyrite as a proxy for fluid source and evolution in the Candelaria-Punta del Cobre iron oxide copper-gold district, Chile. Economic Geology, doi:10.5382/econgeo.4765.

Reich, M., Kesler, S.E., Utsunomiya, S., Palenik, C.S., Chryssoulis, S.L., Ewing, R.C. (2005) Solubility of gold in arsenian pyrite. Geochimica et Cosmochimica Acta, 69, 2781–2796.

Reich, M., Becker, U. (2006) First-principles calculations of the thermodynamic mixing properties of arsenic incorporation into pyrite and marcasite. Chemical Geology, 225, 278–290.

Reich, M., Deditius, A., Chryssoulis, S., Li, J.W., Ma, C.Q., Parada, M.A., Barra, F., Mittermayr, F. (2013) Pyrite as a record of hydrothermal fluid evolution in a porphyry copper system: A SIMS/EMPA trace element study. Geochimica et Cosmochimica Acta, 104, 42–62.

Reich, M., Simon, A., Deditius, A., Barra, F., Chryssoulis, S., Lagas, G., Tardani, D., Knipping, J., Bilenker, L., Sánchez-Alfaro, P., Roberts, M.P., Munizaga, R. (2016) Trace element signature of pyrite from the Los Colorados iron oxide-apatite (IOA) deposit, Chile: A missing link between Andean IOA and iron oxide copper-gold systems?. Economic Geology, 11, 743–761.

Rempel, K.U., Williams-Jones, E.E., Migdisov, A.A. (2009) The partitioning of molybdenum (VI) between aqueous liquid and vapor at temperatures up to 370°C: Geochimica et Cosmochimica Acta, 73, 3381–3392.

Revan, M.K., Genc, Y., Maslennikov, V.V., Maslennikov, S.P., Large, R.R., Danyushevsky, L.V. (2014) Mineralogy and trace element geochemistry of sulfide minerals in hydrothermal chimneys from the Upper-Cretaceous VMS deposits of the Eastern Pontide orogenic belt (NE Turkey). Ore Geology Reviews, 63, 129–149.

Román, N., Reich, M., Leisen, M., Morata, D., Barra, F., Defitius, A.P. (2019) Geochemical and micro-textural fingerprints of boiling in pyrite. Geochimica et Cosmochimica Acta, 246: 60–85.

Rowins, S.M., Groves, D.I., McNaughton, N.J., Palmer, M.R., Eldridge, C.S. (1997) A reinterpretation of the role of granitoids in the genesis of Neoproterozoic gold mineralization in the Telfer dome, western Australia. Economic Geology, 92, 133–160.

Savage, K.S, Tingle, T.N., O'Day, P.A., Waychunas, A. Bird, D.K. (2000) Arsenic speciation in pyrite and secondary weathering phases, Mother Load Gold District, Tuolumne County California. Applied

Geochemistry, 15, 1219–1244.

Seo, J.H., Guillong, M., Heinrich, C.A. (2009) The role of sulfur in the formation of magmatic-hydrothermal copper-gold deposits. Earth and Planetary Science Letters, 282, 323–328.

Seo, J.H., Guillong, M., Heinrich, C.A. (2012) Separation of molybdenum and copper in porphyry deposits: The roles of sulfur, redox, and pH in ore mineral deposition at Bingham Canyon. Economic Geology, 107, 333–356.

Shu, Q.A., Chen, P.L., Cheng, J.R. (1992) Geology of Iron-Copper Deposits in Eastern Hubei Province, China. Beijing: Metallurgic Industry Press, 192 p (in Chinese).

Sibson, R.H., Robert, F., Poulsen, K.H. (1988) High-angle reverse faults, fluid-pressure cycling, and mesothermal gold-quartz deposits. Geology, 16, 551–555.

Simmons, S.F., Browne, P.R.L. (2000) Hydrothermal minerals and precious metals in the Broadlands-Ohaaki geothermal system: implications for understanding low-sulfidation epithermal environments. Economic Geology, 95, 971–999.

Smith, J.W., Holwell, D.A., McDonald, I. (2014) Precious and base metal geochemistry and mineralogy of the Grasvally Norite-Pyroxenite-Anorthosite (GNPA) member, northern Bushveld Complex, South Africa: implications for a multistage emplacement. Mineralium Deposita, 49, 667–692.

Spycher, N.F., Reed, M.H. (1989) Evolution of a Broadlands-type epithermal ore fluid along alternative P-T paths: implications for the transport and deposition of base, precious, and volatile metals. Economic Geology, 84, 328–359.

Sun, S.Q., Chen, H.Y., Jin, S.G., Wei, K.T., Zhang, S.T., Zhang, Y. (2019) Geochemistry of altered minerals and its application in Edong ore district, China. Science Press, Beijing, 255 p (in Chinese).

Sykora, S., Cooke, D.R., Meffre, S., Stephanov, A.S., Gardner, K., Scott, R., Selley, D., Harris, A.C. (2018) Evolution of pyrite trace element compositions from porphyry-style and epithermal conditions at the Lihir gold deposit: Implications for ore genesis and mineral processing. Economic Geology, 113, 193–208.

Tanner, D., Henley, R.W., Mavrogenes, J.A., Holden, P. (2016) Sulfur isotope and trace element systematics of zoned pyrite crystals from the El Indio Au–Cu–Ag deposit, Chile. Contributions to Mineralogy and Petrology, 171, 33.

Thomas, H.V., Large, R.R., Bull, S.W., Maslennikov, V., Berry, R.F., Fraser, R., Froud, S., Moye, R. (2011) Pyrite and pyrrhotite textures and composition in sediments, laminated quartz veins, and reefs at Bendigo gold mine, Australia: insights for ore genesis. Economic Geology, 106, 1–31.

Tian, J., Zhang, Y., Cheng, J.M., Sun, S.Q., Zhao, Y.J. (2019) Short wavelength infra-red (SWIR) characteristics of hydrothermal alteration minerals in skarn deposits: Example from the Jiguanzui Cu–Au deposit, Eastern China. Ore Geology Reviews, 106, 134–149.

Tribovillard, N., Algeo, T.J., Lyons, T., Riboulleau, A. (2006) Trace metals as paleoredox and paleoproductivity proxies: an update. Chemical Geology, 232, 12–32.

Voute, F., Hagemann, S.G., Evans, N.J., Villanes, C. (2019) Sulfur isotopes, trace element, and textural analyses of pyrite, arsenopyrite and base metal sulfides associated with gold mineralization in the Pataz-Parcoy district, Peru: implication for paragenesis, fluid source, and gold deposition mechanisms. Mineralium Deposita, 54, 1077–1100.

Williams, M.R., Holwell, D.A., Lilly, R.M., Case, G.N.D., McDonald, I. (2015) Mineralogical and fluid characteristics of the fluorite-rich Monakoff and E1 Cu-Au deposits, Cloncurry region, Queensland, Australia: implications for regional F-Ba-rich IOCG mineralization. Ore Geology Reviews, 64, 103–127.

Wohlgemuth-Ueberwasser, C.C., Viljoen, F., Petersen, S., Vorster, C. (2015) Distribution and solubility limits of trace elements in hydrothermal black smoker sulfides: an in-situ LA-ICP-MS study. Geochimica et Cosmochimica Acta, 159, 16–41.

Wu, Y.F., Li, J.W., Evans, K., Koenig, A.E., Li, Z.K., O'Brien, H., Lahaye, Y., Rempel, K., Hu, S.Y., Zhang, Z.P., Yu, J.P. (2018), Ore-forming processes of the Daqiao epizonal orogenic gold deposit, West Qinling Orogen, China: constraints from textures, trace elements, and sulfur isotopes of pyrite and marcasite, and Raman spectroscopy of carbonaceous material. Economic Geology, 113, 1093–1132.

Xie, G.Q., Mao, J.W., Li, R.L., Jiang, G.H., Zhao, C.S., Zhao, H.J., Hou, K.J., Pan, H.J. (2008) ^{40}Ar-^{39}Ar phlogopite dating of large skarn Fe deposits and tectonic framework in southeastern Hubei Province, Middle-Lower Reaches of the Yangtze River, eastern China. Acta Petrological Sinica, 24(8), 1917–1927.

Xie, G.Q., Mao, J.W., Zhao, H.J. (2011a) Zircon U–Pb geochronological and Hf isotopic constraints on petrogenesis of Late Mesozoic intrusions in the southeast Hubei Province, Middle-Lower Yangtze River belt (MLYRB), East China. Lithos, 125, 693–710.

Xie, G.Q., Mao, J.W., Zhao, H.J., Wei, K.T., Jin, S.G., Pan, H.J., Ke, Y.F. (2011b) Timing of skarn deposit formation of the Tonglushan ore district, southeastern Hubei Province, Middle–Lower Yangtze River Valley metallogenic belt and its implications. Ore Geology Reviews, 43, 62–77.

Xie, G.Q., Mao, J.W., Zhao, H.J., Duan, C., Yao, L. (2012) Zircon U–Pb and phlogopite ^{40}Ar–^{39}Ar age of the Chengchao and Jinshandian skarn Fe deposits, southeast Hubei Province, Middle-Lower Yangtze River Valley metallogenic belt, China. Mineralium Deposita, 47, 633–652.

Zhang, W. (2015) Ore genesis of the Jiguanzui Cu–Au deposit in Southeastern Hubei Province, China. China University of Geosciences Press, Wuhan, 127 p (in Chinese).

Zhang, W., Wang, H.Q., Li, J.W., Deng, X.D., Hu, H., Li, J.W. (2016) Mineralogy of the Au-Ag-Bi-Te-Se assemblages in the Jiguanzui Cu-Au skarn deposit, Daye District, southeastern Hubei Province. Acta Petrologica Sinica, 32(2), 456–470 (in Chinese with English abstract).

Zhang, Y., Shao, Y.J., Wu, C.D., Chen, H.Y. (2017a) LA-ICP-MS trace element geochemistry of garnets: Constraints on hydrothermal fluid evolution and genesis of the Xinqiao Cu–S–Fe–Au deposit, eastern China. Ore Geology Reviews, 86, 426–439.

Zhang, Y., Shao, Y.J., Li, H.B., Liu, Z.F. (2017b) Genesis of the Xinqiao Cu–S–Fe–Au deposit in the Middle-Lower Yangtze River Valley metallogenic belt, Eastern China: Constraints from U–Pb–Hf, Rb–Sr, S, and Pb isotopes. Ore Geology Reviews, 86, 100–116.

Zhang, Y., Shao, Y.J., Chen, H.Y., Liu, Z.F., Li, D.F. (2017c) A hydrothermal origin for the large Xinqiao Cu-S-Fe deposit, Eastern China: Evidence from sulfide geochemistry and sulfur isotopes. Ore Geology Reviews, 88, 534–549.

Zhang, Y., Shao, Y.J., Zhang, R.Q., Li, D.F., Liu, Z.F., Chen, H.Y. (2018) Dating ore deposit using garnet U–Pb geochronology: Example from the Xinqiao Cu–S–Fe–Au deposit, Eastern China. Minerals, 8, 31.

Zhang, Y., Cheng, J.M., Tian, J., Pan, J., Sun, S.Q., Zhang, L.J., Zhang, S.T., Chu, G.B., Zhao, Y.J., Lai, C. (2019) Texture and trace element geochemistry of quartz in skarn system: Perspective from Jiguanzui Cu–Au skarn deposit, Eastern China. Ore Geology Reviews, 109, 534–544.

Figure captions

Fig. 1. (a) Location of the Edong ore district in the MLYRB, Eastern China (modified after Xie et al. 2011a and Zhang et al. 2019). TLF: Tancheng – Lujiang fault; XGF: Xiangfan – Guangji fault;

YCF: Yangxing – Changzhou fault; (b) Geologic map of the Edong ore district, showing the major types of skarn deposits (modified after Shu et al. 1992; Li et al. 2008; Xie et al. 2011b).

Fig. 2. (a) Geologic map of the Jiguanzui deposit and (b) geological section of the Jiguanzui deposit (modified after Ke et al. 2016 and Zhang et al. 2016, 2019).

Fig. 3. Paragenetic sequence of the Jiguanzui Au–Cu deposit (modified after Tian et al. 2019).

Fig. 4. Photographs showing representative mineral assemblages and textures of Py1. (a) Py1a intergrown with anhedral quartz and chalcopyrite in Orebody VII; (b) Intergranular replacement of garnet by Py1a; (c) Py1a replaced early magnetite; (d) Quartz with miarolitic cavities in quartz–Py1a vein hosted in hornfels; (e) Typical quartz–Py1a–chalcopyrite–molybdenite vein in hornfels; (f) Quartz–Py1a vein cut by calcite–pyrite (Py2a) stockwork. (g) Quartz–Py1a wavy selvage hosted in the Puqi Fm. hornfels; (h) Irregular clump of quartz–Py1a in hornfels; (i) Anhedral Py1b coexists with quartz and calcite in Orebody VII; (j) Quartz–calcite–molybdenite–Py1b vein in hornfels; (k) Calcite–pyrite vein cuts through the quartz–calcite–pyrite clump in hornfels, indicating that Py1b formed before pyrite (which only coexists with calcite); (l) Quartz–calcite–Py1b vein cuts quartz–Py1a vein, indicating the earlier formation of Py1a than Py1b; (m) Irregular clump of quartz–sericite–Py1c in hornfels; (n) Subhedral-euhedral Py1c grain coexists with quartz and sericite (CPL); (o) Irregular hematite in hornfels replaced by Py1c and intergrown with quartz and sericite; (p) Typical alteration halo (discoloration) of quartz–chlorite–

Py1d vein in hornfels; (q) Quartz confined on the both sides of quartz–chlorite–Py1d vein (PPL); (r) Clumps of quartz–chlorite–epidote–Py1d in hornfels; (s) Wavy quartz–K-feldspar–Py1e vein in quartz diorite with K-feldspar alteration halo; (t) Straight quartz–K-feldspar–Py1e vein in hornfels.

Abbreviations: Qz = quartz; Grt = garnet; Cal = calcite; Kfs = K-feldspar; Ser = sericite; Chl = chlorite; Ep = epidote; Mag = magnetite; Ccp = chalcopyrite; Mol = molybdenite; Py = pyrite; Hem = hematite.

Fig. 5. Photographs showing representative mineral assemblages and textures of Py2 and Py3. (a) Subhedral-euhedral Py2a grains coexist with massive calcite in Orebody VII; (b) Py2a coexists with sphalerite and galena in Orebody VII; (c) Calcite–Py2a veins with different pyrite/calcite ratios hosted in the Puqi Fm. hornfels; (d) Typical straight-side calcite–Py2a vein with obvious wavy discolored selvage; (e) Curvy calcite–Py2a vein in dolomitic marble with a calcite centerline; (f) Typical subhedral-euhedral Py2a in calcite–Py2a vein; (g) Local discontinuous Py2a sub-veins in calcite–Py2a vein; (h) Py2a confined on both sides by calcite–Py2a stockworks in hornfels; (i) Py2a intergrown with calcite in calcite–Py2a stockworks that intruded dolomitic marble; (j) Calcite–Py2a veins cut clumps of quartz–sericite–Py1c; (k) Calcite–Py2a veins cut quartz–chlorite–Py1d vein; (l) Typical clumps of calcite–K-feldspar–Py2b in hornfels; (m) Typical calcite–K-feldspar–Py2b vein in hornfels; (n) Hand-specimen of porous Py3a and Py3b; (o) Py3a with irregular bird's-eye texture replaced Py1b, and coexists with quartz and calcite along fracture; (p) Py3b pseudomorph resulted from the recrystallization to Py3a. Abbreviations

as in Figure 3 and Sp = sphalerite; Gn = galena.

Fig. 6. Representative BSE images of the Jiguanzui pyrite grain. (a) Py1a with telluride inclusions shows homogeneous texture; (b) Bismuthide inclusion in Py1a; (c) Fractured Py1b grain; (d) Quartz inclusion-bearing Py1c grain; (e) Fractured Py1d grain in quartz–chlorite–Py1d vein that intruded hornfels; (f) Anhedral K-feldspar inclusions in Py1e; (g) Sphalerite inclusions Py2a; (h) Anhedral Py2b grain; (i) Py1c grain with slightly-zoned texture. Abbreviations as in Figure 3 and Te = telluride; Bi = bismuthide.

Fig. 7. Representative LA-ICP-MS time-resolved signals of the Jiguanzui pyrite.

Fig. 8. Box and whisker plot for the trace element concentrations of the nine types of Jiguanzui pyrite. The geometric mean (dot), median (horizontal line), first quartile (Q1, lower limit of the box) and third quartile (Q3, upper limit of the box) are shown. Outlier values are shown as triangles and circles (see legend for details).

Fig. 9. Binary diagrams of trace elements in the Jiguanzui pyrite: (a) Au vs. As (Au solubility line after Reich et al. 2005) and (b) Co vs. Ni.

Fig. 10. Schematic diagram for the Jiguanzui skarn ore formation. (a) Formation of abundant CO_2 during the conversion of carbonate to skarn in the prograde and retrograde stages, markedly

increasing the pressure of fluids in the contact between the Jialingjiang Fm.dolomitic marble and the intruding quartz diorite; (b) Stress accumulation caused extensive hydraulic fracturing of wallrocks when the rising fluid pressure gradually exceeded the lithostatic load in the early main ore-forming stage, which triggered phase separation, fluid boiling, and the removal of acidic volatile components, coupled with fO_2 and pH increase of “boiled” waters; (c) Mineralization formed in the contact between the Jialingjiang Fm.dolomitic marble and the intruding quartz diorite because of phase separation and fluid boiling in the late main ore-forming stage, and the pyrite veins/clumps in wallrocks were formed after the fracture sealing; (d) Hydraulic fracturing of the wallrocks provided fluid conduits for meteoric water influx, and promoted fluid mixing between meteoric water and magmatic-hydrothermal fluids, which was responsible for the metal sulfide precipitation in the late ore stage and the post-ore Py3 formation.

Fig. 11. Trace-element concentration contour diagrams for Py1a cross-section. (a) Cross-section of the area covered by the contour map. Legends as in Figure 2. (b) As; (c) Se; (d) Co; (e) Ni.

Table caption

Table 1. Statistics of trace element composition data of the Jiguanzui pyrite (ppm).

Table 1. Summary of statistics for trace-element data set of the Jiguanzui pyrite (ppm).

Type	Statistics	Co	Ni	Cu	Zn	As	Se	Mo	Ag	Te	Au	Pb	Bi
Py1	n	731	730	464	648	683	724	314	291	573	510	600	609
	Min	0.005	0.011	0.147	0.213	0.640	3.32	0.002	0.012	0.046	0.001	0.003	0.001
	Max	14691	4763	3365	101	7016	1110	204	54.8	913	13.5	289	270
	Ave	320	121	30.9	1.56	155	76.5	1.02	0.937	18.8	0.166	5.40	4.33
	Median	38.7	30.1	1.19	0.498	9.45	50.5	0.010	0.128	1.88	0.027	0.191	0.202
	MAD	38.2	29.0	0.850	0.140	7.53	31.7	0.010	0.100	1.74	0.020	0.180	0.200
Py1a (orebodies)	n	164	160	99	147	159	169	61	71	143	115	130	139
	Min	0.005	0.011	0.167	0.255	0.754	3.32	0.002	0.016	0.070	0.002	0.004	0.001
	Max	4755	4763	134	44.0	2847	461	39.7	54.8	356	1.69	193	270
	Ave	163	93.4	7.58	1.71	299	64.2	0.720	1.89	21.5	0.11	6.73	7.52
	Median	14.1	10.5	1.21	0.482	58.2	37.9	0.010	0.207	6.82	0.027	0.245	0.453
	MAD	14.0	10.4	0.860	0.100	53.0	26.2	0.010	0.180	5.86	0.020	0.240	0.450
Py1a (wall rocks)	n	411	411	254	361	369	407	187	156	310	286	338	334
	Min	0.009	0.025	0.158	0.213	0.640	3.60	0.002	0.014	0.049	0.002	0.003	0.001
	Max	12141	3202	3365	101	4755	1110	204	13.3	913	5.53	203	129
	Ave	266	121	50.3	1.79	85.6	89.1	1.46	0.700	18.4	0.108	3.89	3.43
	Median	49.6	34.1	1.24	0.488	7.05	60.8	0.009	0.101	1.04	0.029	0.140	0.190
	MAD	48.4	31.8	0.890	0.150	5.13	37.0	0.010	0.080	0.920	0.020	0.130	0.190
Py1b	n	17	20	19	21	20	18	17	12	18	18	19	17
	Min	0.097	0.194	0.375	0.326	0.757	9.41	0.003	0.022	0.090	0.003	0.036	0.004
	Max	6810	1564	85.6	1.63	7016	494	0.308	10.2	272	13.5	289	54.4
	Ave	626	178	13.8	0.79	1033	117	0.044	1.43	45.8	1.91	45.2	8.97
	Median	65.9	6.55	4.82	0.655	13.0	49.7	0.023	0.209	15.2	0.056	0.628	0.202
	MAD	65.7	6.32	4.03	0.220	10.4	22.5	0.010	0.180	14.6	0.050	0.530	0.200
Py1c	n	12	12	10	10	12	12	4	2	9	9	10	11
	Min	26.2	26.9	0.157	0.332	1.09	9.34	0.009	0.164	0.107	0.002	0.025	0.002
	Max	378	1246	7.02	0.76	23.5	68.5	0.105	0.226	3.11	0.028	25.5	10.8
	Ave	98.4	355	1.33	0.531	9.38	25.2	0.033	0.195	1.06	0.012	2.77	2.05
	Median	67.0	123	0.418	0.535	8.21	16.8	0.009	0.195	0.579	0.011	0.205	0.377
	MAD	31.0	95.3	0.250	0.160	4.36	3.78	0.004	0.030	0.430	0.004	0.180	0.370
Py1d	n	35	35	30	34	35	27	19	16	21	27	29	28
	Min	2.14	4.35	0.15	0.29	1.41	4.28	0.003	0.012	0.046	0.003	0.009	0.002
	Max	14691	290	7.48	7.33	35.7	36.3	0.070	0.310	26.3	0.685	8.66	3.68
	Ave	1886	92.9	1.19	1.36	6.09	13.9	0.026	0.102	2.24	0.102	0.959	0.302
	Median	889	77.4	0.55	0.61	3.44	8.86	0.019	0.076	0.585	0.067	0.175	0.038
	MAD	835	52.5	0.36	0.23	0.96	3.59	0.010	0.050	0.360	0.060	0.140	0.030
Py1e	n	92	92	52	75	88	91	26	34	72	55	74	80
	Min	0.056	0.038	0.295	0.232	1.117	3.98	0.002	0.018	0.074	0.001	0.004	0.002
	Max	2900	1903	238	4.08	978	289	0.895	3.68	266	1.26	38.1	37.7
	Ave	220	137	9.77	0.611	63.4	60.4	0.080	0.304	15.4	0.070	1.82	3.30
	Median	45.1	58.5	1.48	0.490	8.11	49.2	0.012	0.120	2.49	0.021	0.222	0.213
	MAD	44.1	57.0	0.980	0.080	4.65	26.9	0.010	0.090	2.22	0.010	0.210	0.210
Py2	n	38	40	30	37	40	37	24	20	26	30	38	29
	Min	0.008	0.013	0.185	0.243	2.01	3.25	0.003	0.016	0.083	0.002	0.003	0.001
	Max	1045	1235	2159	139	9827	95.1	313	8.20	49.4	6.15	31.2	14.6
	Ave	150	68.3	79.0	12.7	838	23.1	42.9	0.583	8.33	0.289	2.21	1.320
	Median	4.10	13.4	0.995	0.575	138	13.6	3.22	0.079	2.71	0.035	0.157	0.272
	MAD	4.00	13.3	0.750	0.230	136	8.94	3.22	0.064	2.57	0.030	0.150	0.270
Py2a	n	20	22	16	22	22	20	17	10	8	15	21	12
	Min	0.008	0.013	0.185	0.251	2.01	3.25	0.003	0.016	0.083	0.002	0.003	0.001
	Max	844	215	2159	139	3519	95.1	313	8.20	49.4	0.568	31.2	0.853
	Ave	137	22.0	147	20.9	555	21.2	60.1	1.05	6.82	0.074	2.67	0.163
	Median	0.917	0.428	7.16	5.00	24.9	19.6	8.06	0.082	0.893	0.024	0.153	0.027
	MAD	0.880	0.400	6.72	4.71	22.5	11.9	8.05	0.064	0.790	0.021	0.147	0.025
Py2b	n	18	18	14	15	18	17	7	10	18	15	17	17
	Min	0.480	1.79	0.224	0.243	2.09	5.00	0.009	0.022	0.146	0.005	0.004	0.003
	Max	1045	1235	4.55	1.73	9827	87.5	6.10	0.310	34.0	6.15	13.5	14.6
	Ave	164	125	1.12	0.608	1183	25.3	0.979	0.116	9.00	0.505	1.65	2.14
	Median	26.7	28.4	0.587	0.512	351	10.4	0.030	0.061	5.28	0.072	0.193	0.577

	MAD	25.1	13.2	0.240	0.070	348	4.43	0.020	0.040	4.46	0.070	0.180	0.440
Py3	n	32	32	32	32	32	32	32	32	32	32	32	32
	Min	82.1	2.80	1188	0.792	49.6	20.5	2.31	3.64	0.508	0.026	2.24	0.043
	Max	1641	601	7279	101	817	58.4	148	18.8	32.6	12.9	74.3	12.0
	Ave	314	115	4826	29.3	421	41.2	40.7	11.7	6.70	0.591	24.1	1.06
	Median	201	33.5	5124	23.6	457	42.6	40.5	11.3	4.66	0.183	21.4	0.234
	MAD	103	29.8	532	13.5	113	4.26	23.8	3.87	2.87	0.090	8.68	0.150
Py3a	n	19	19	19	19	19	19	19	19	19	19	19	19
	Min	106	29.7	2012	5.64	145	20.5	18.4	4.13	0.508	0.026	11.6	0.125
	Max	1641	601	7279	78.3	817	58.4	148	16.4	32.6	12.9	74.3	12.0
	Ave	465	191	4922	20.5	384	40.4	60.7	10.1	4.17	0.868	27.1	1.64
	Median	262	174	5347	17.6	357	41.0	56.1	10.4	2.19	0.210	18.9	0.387
	MAD	63.8	122	789	10.7	124	2.46	7.11	1.36	1.15	0.130	5.62	0.240
Py3b	n	13	13	13	13	13	13	13	13	13	13	13	13
	Min	82.1	2.80	1188	0.792	49.6	30.3	2.31	3.64	6.44	0.053	2.24	0.043
	Max	137	4.79	6058	101	646	50.6	17.3	18.8	17.5	0.528	34.4	0.781
	Ave	95.0	3.73	4686	42.2	475	42.4	11.4	14.1	10.4	0.187	19.7	0.224
	Median	89.3	3.65	5080	37.3	506	46.3	13.2	15.1	9.19	0.175	27.1	0.165
	MAD	5.48	0.460	536	25.5	65.3	3.12	3.42	2.16	1.64	0.070	6.92	0.110

Abbreviations: Min = minimum; Max = maximum; Ave = average; MAD = Median absolute deviation.

Fig. 1

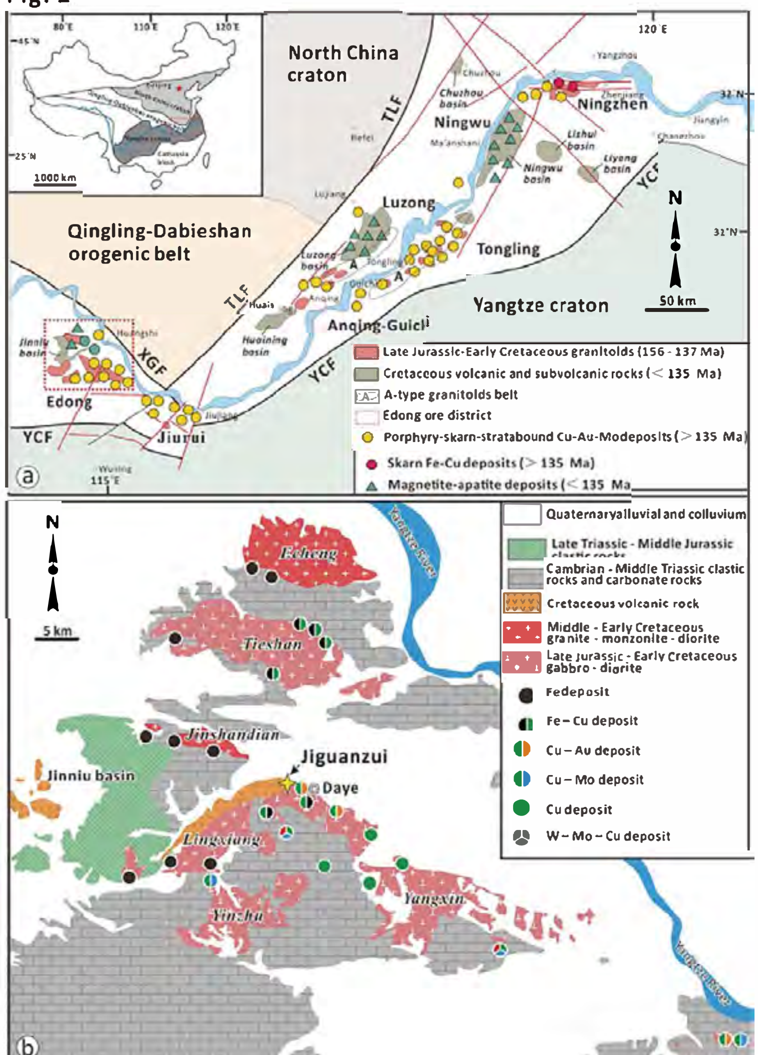
North China craton
Qingling-Dabieshan orogenic belt
Yangtze craton
TLF
XGF
YCF
Ningwu
Ningzhen
Luzong
Tongling
Anqing-Guichi
Edong
Jiurui
50 km
1000 km
Late Jurassic-Early Cretaceous granitoids (156 - 137 Ma)
Cretaceous volcanic and subvolcanic rocks (< 135 Ma)
A-type granitoids belt
Edong ore district
Porphyry-skarn-stratabound Cu-Au-Modeposits (> 135 Ma)
Skarn Fe-Cu deposits (> 135 Ma)
Magnetite-apatite deposits (< 135 Ma
(a)
N
5 km
Quaternaryalluvial and colluvium
Late Triassic - Middle Jurassic clastic rocks
Cambrian - Middle Triassic clastic rocks and carbonate rocks
Cretaceous volcanic rock
Middle - Early Cretaceous granite - monzonite - diorite
Late Jurassic - Early Cretaceous gabbro - diorite
Fedeposit
Fe - Cu deposit
Cu - Au deposit
Cu - Mo deposit
Cu deposit
W - Mo - Cu deposit
Echeng
Tieshan
Jinshandian
Jiguanzui
Daye
Jinniu basin
Lingxiang
Yinzhu
Yangxin
(b)

Fig. 2

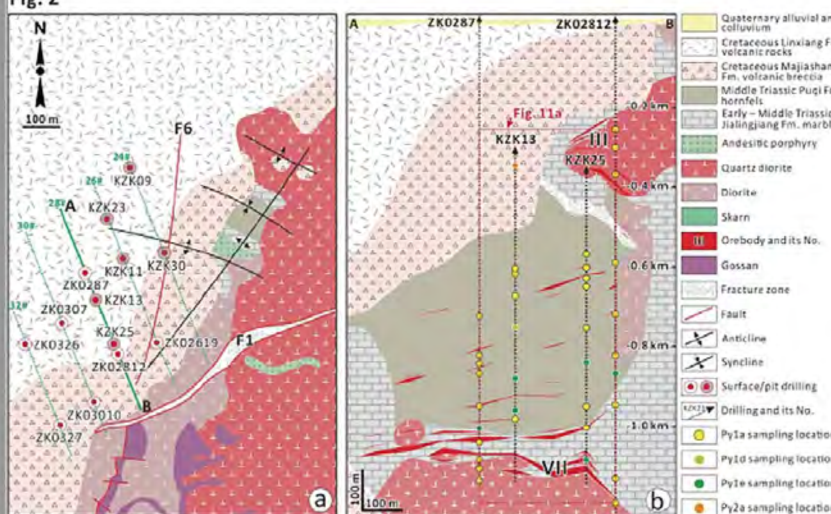
N
100 m
F6
F1
A
B
KZK09
KZK23
KZK11
KZK30
ZK0287
KZK13
ZK0307
ZK0326
KZK25
ZK02619
ZK02812
ZK03010
ZK0327
a
ZK0287
ZK02812
Fig. 11a
KZK13
KZK25
III
VII
-0.2 km
-0.4 km
-0.6 km
-0.8 km
-1.0 km
100 m
b
Quaternary alluvial and colluvium
Cretaceous Linxiang Fm. volcanic rocks
Cretaceous Majiashan Fm. volcanic breccia
Middle Triassic Puqi Fm. hornfels
Early – Middle Triassic Jialingjiang Fm. marble
Andesitic porphyry
Quartz diorite
Diorite
Skarn
Orebody and its No.
Gossan
Fracture zone
Fault
Anticline
Syncline
Surface/pit drilling
Drilling and its No.
Py1a sampling location
Py1d sampling location
Py1e sampling location
Py2a sampling location

Fig. 3

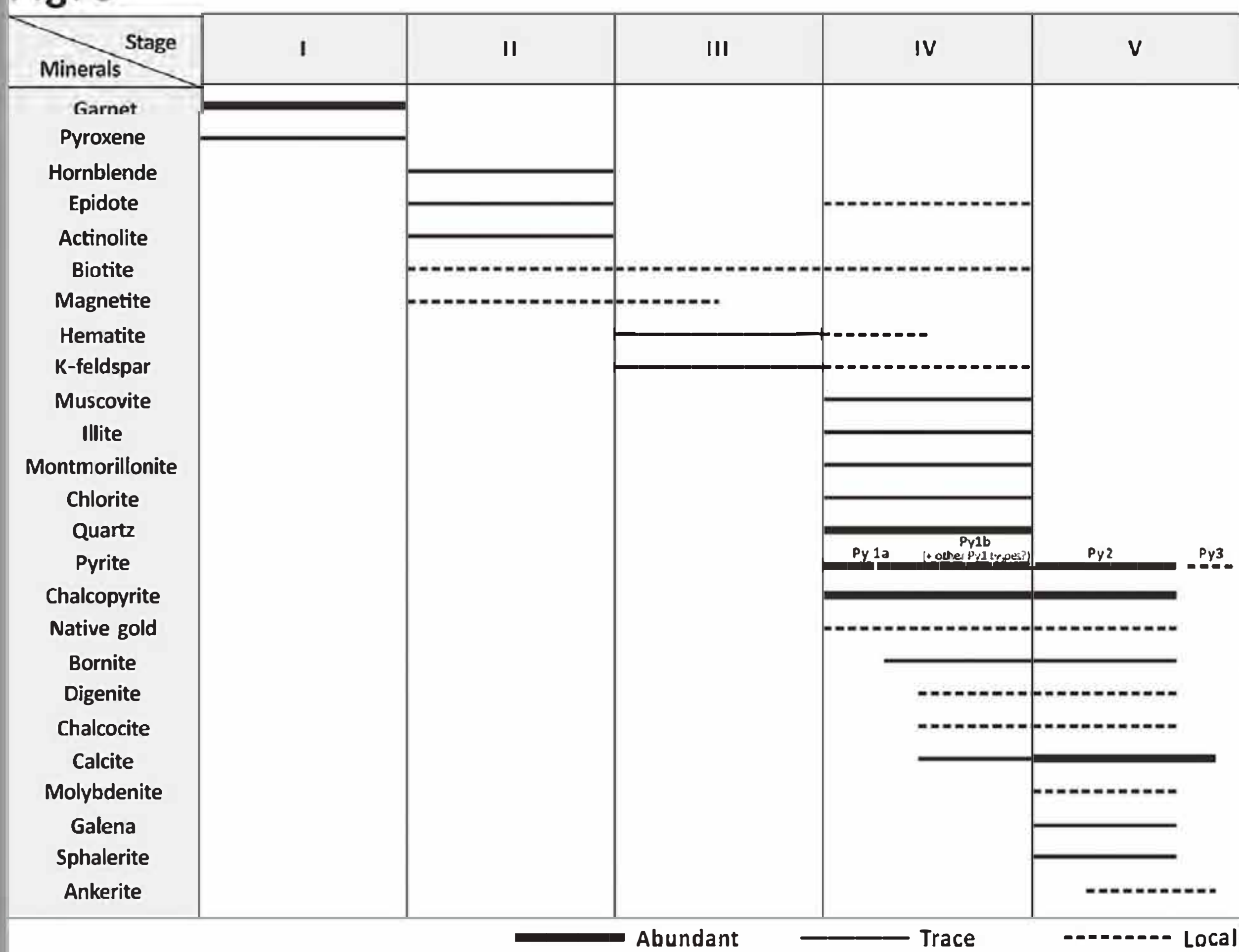
Stage
Minerals
I
II
III
IV
V
Garnet
Pyroxene
Hornblende
Epidote
Actinolite
Biotite
Magnetite
Hematite
K-feldspar
Muscovite
Illite
Montmorillonite
Chlorite
Quartz
Pyrite
Chalcopyrite
Native gold
Bornite
Digenite
Chalcocite
Calcite
Molybdenite
Galena
Sphalerite
Ankerite
Py 1a
Py1b
(+ other Py1 types?)
Py2
Py3
Abundant
Trace
Local

Fig. 4

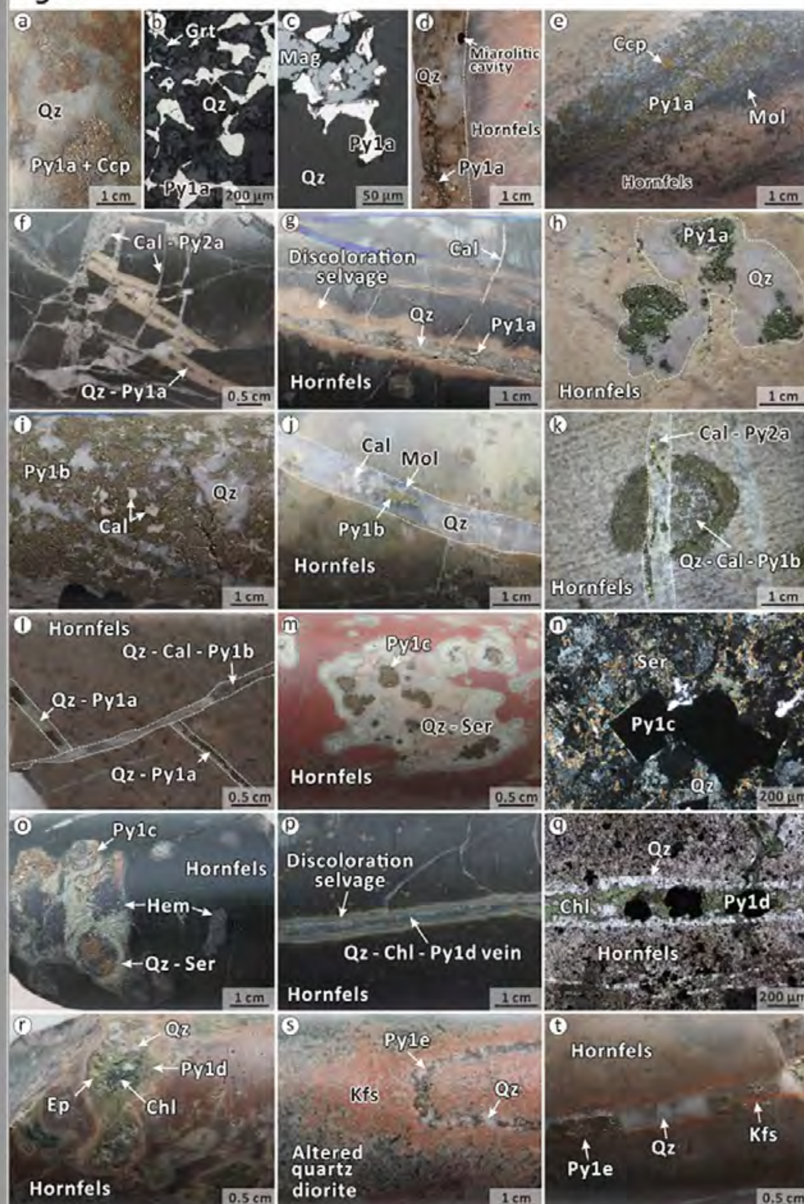

a
Qz
Py1a + Ccp
1 cm
b
Grt
Qz
Py1a
200 µm
c
Mag
Py1a
Qz
50 µm
d
Miarolitic cavity
Qz
Hornfels
Py1a
1 cm
e
Ccp
Py1a
Mol
Hornfels
1 cm
f
Cal - Py2a
Qz - Py1a
0.5 cm
g
Discoloration selvage
Cal
Qz
Py1a
Hornfels
1 cm
h
Py1a
Qz
Hornfels
1 cm
i
Py1b
Qz
Cal
1 cm
j
Cal
Mol
Py1b
Qz
Hornfels
1 cm
k
Cal - Py2a
Qz - Cal - Py1b
Hornfels
1 cm
l
Hornfels
Qz - Cal - Py1b
Qz - Py1a
Qz - Py1a
0.5 cm
m
Py1c
Qz - Ser
Hornfels
0.5 cm
n
Ser
Py1c
Qz
200 µm
o
Py1c
Hornfels
Hem
Qz - Ser
1 cm
p
Discoloration selvage
Qz - Chl - Py1d vein
Hornfels
1 cm
q
Qz
Chl
Py1d
Hornfels
200 µm
r
Qz
Py1d
Ep
Chl
Hornfels
0.5 cm
s
Py1e
Kfs
Qz
Altered quartz diorite
1 cm
t
Hornfels
Py1e
Qz
Kfs
0.5 cm

Fig. 5

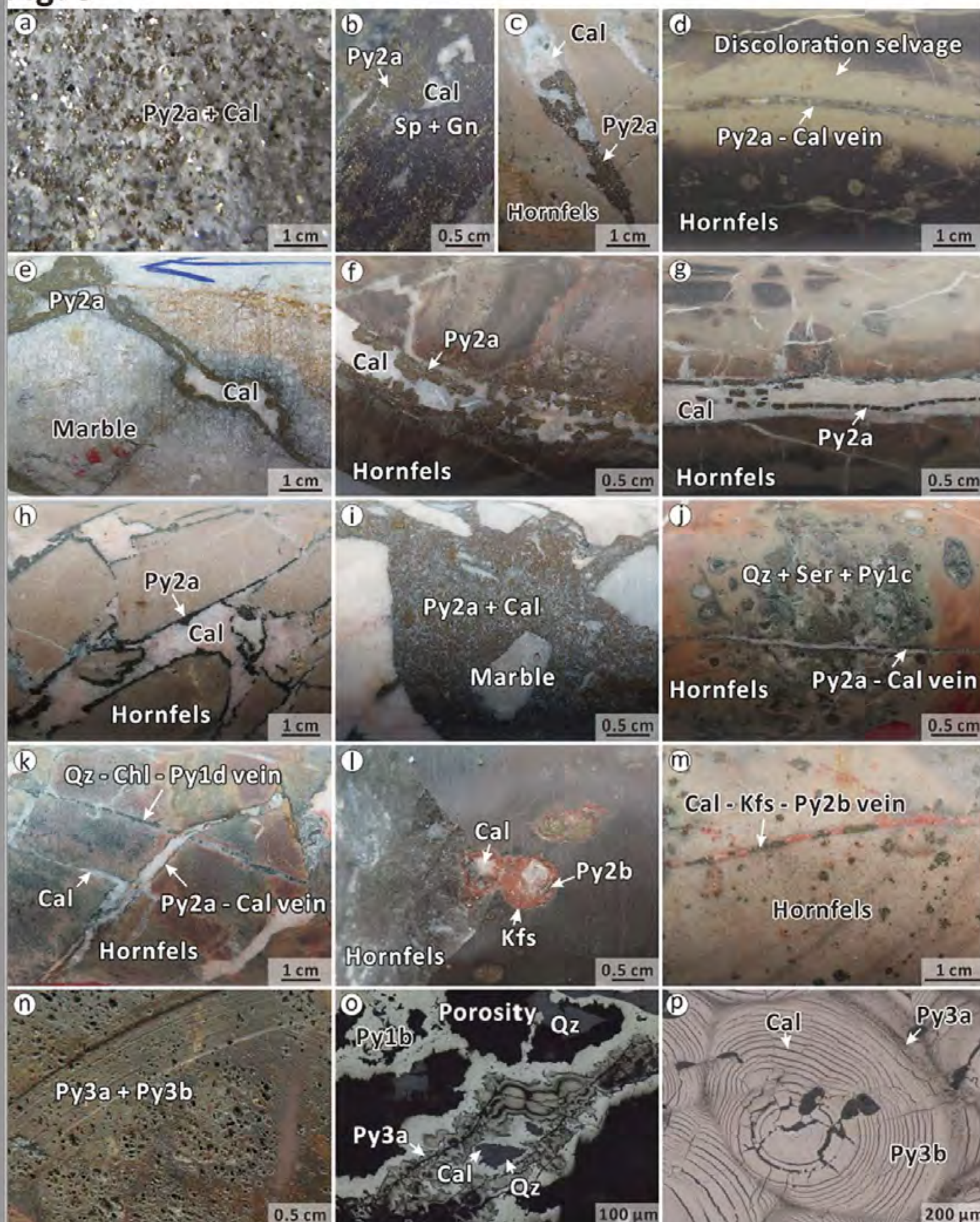
a
Py2a + Cal
1 cm
b
Py2a
Cal
Sp + Gn
0.5 cm
c
Cal
Py2a
Hornfels
1 cm
d
Discoloration selvage
Py2a - Cal vein
Hornfels
1 cm
e
Py2a
Cal
Marble
1 cm
f
Py2a
Cal
Hornfels
0.5 cm
g
Cal
Py2a
Hornfels
0.5 cm
h
Py2a
Cal
Hornfels
1 cm
i
Py2a + Cal
Marble
0.5 cm
j
Qz + Ser + Py1c
Hornfels
Py2a - Cal vein
0.5 cm
k
Qz - Chl - Py1d vein
Cal
Py2a - Cal vein
Hornfels
1 cm
l
Cal
Py2b
Kfs
Hornfels
0.5 cm
m
Cal - Kfs - Py2b vein
Hornfels
1 cm
n
Py3a + Py3b
0.5 cm
o
Porosity
Qz
Py1b
Py3a
Cal
Qz
100 µm
p
Cal
Py3a
Py3b
200 µm

Fig. 6

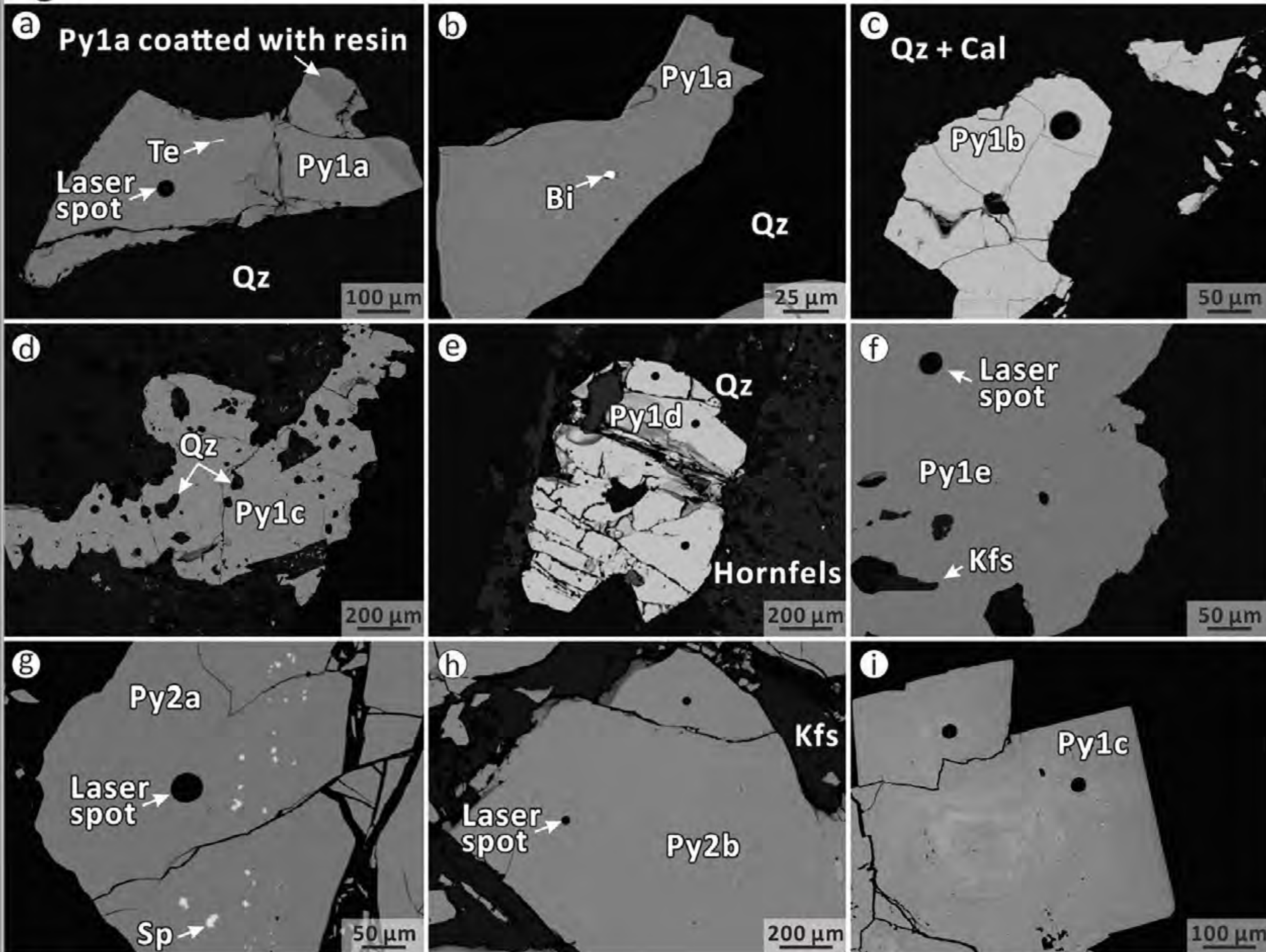
a
Py1a coatted with resin
Te
Laser spot
Py1a
Qz
100 µm
b
Py1a
Bi
Qz
25 µm
c
Qz + Cal
Py1b
50 µm
d
Qz
Py1c
200 µm
e
Qz
Py1d
Hornfels
200 µm
f
Laser spot
Py1e
Kfs
50 µm
g
Py2a
Laser spot
Sp
50 µm
h
Kfs
Laser spot
Py2b
200 µm
i
Py1c
100 µm

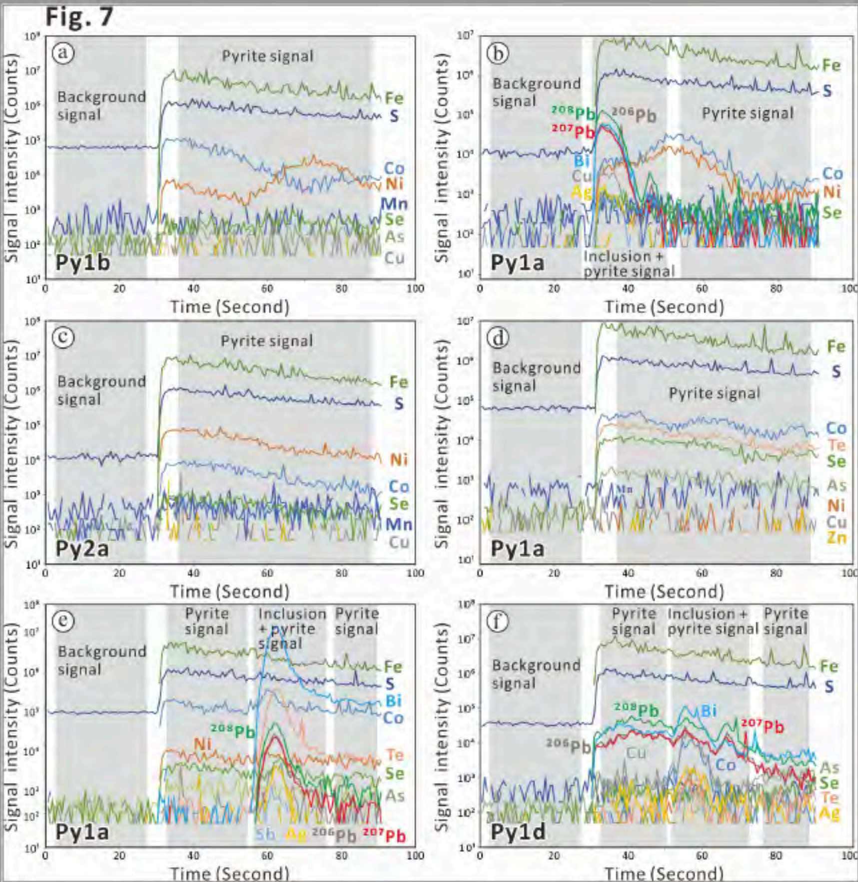

Fig. 7
a
Pyrite signal
Background signal
Fe
S
Co
Ni
Mn
Se
As
Cu
Py1b
b
Background signal
Pyrite signal
Inclusion + pyrite signal
208Pb
206Pb
207Pb
Bi
Cu
Ag
Fe
S
Co
Ni
Se
Py1a
c
Pyrite signal
Background signal
Fe
S
Ni
Co
Se
Mn
Cu
Py2a
d
Background signal
Pyrite signal
Fe
S
Co
Te
Se
As
Ni
Cu
Zn
Py1a
e
Background signal
Pyrite signal
Inclusion + pyrite signal
Pyrite signal
208Pb
Ni
Fe
S
Bi
Co
Te
Se
As
Sb
Ag
206Pb
207Pb
Py1a
f
Background signal
Pyrite signal
Inclusion + pyrite signal
Pyrite signal
208Pb
Bi
207Pb
206Pb
Cu
Co
Fe
S
As
Se
Te
Ag
Py1d
Signal intensity (Counts)
Time (Second)

Fig. 8

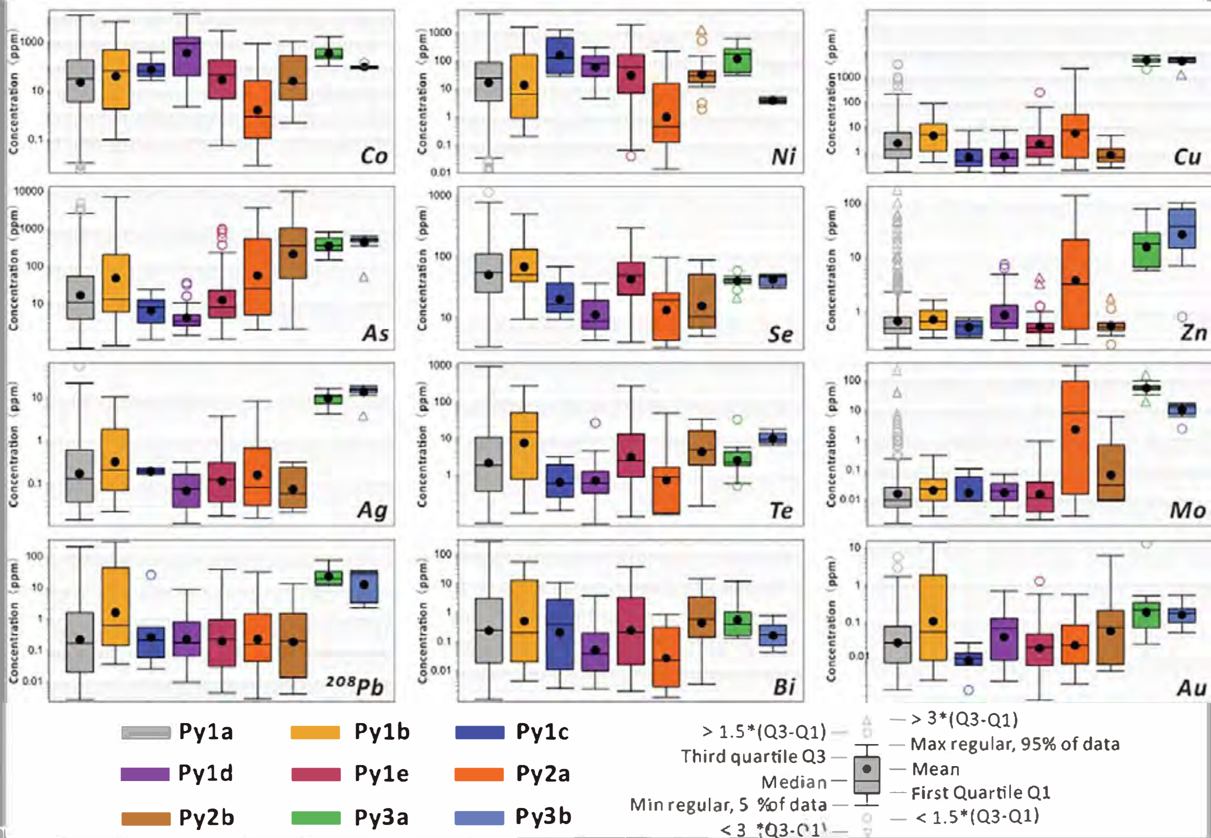

Co
Ni
Cu
As
Se
Zn
Ag
Te
Mo
208Pb
Bi
Au
Concentration (ppm)
Py1a
Py1b
Py1c
Py1d
Py1e
Py2a
Py2b
Py3a
Py3b
> 3*(Q3-Q1)
> 1.5*(Q3-Q1)
Max regular, 95% of data
Third quartile Q3
Mean
Median
First Quartile Q1
Min regular, 5 %of data
< 1.5*(Q3-Q1)
< 3 *(Q3-Q1)

Fig.9

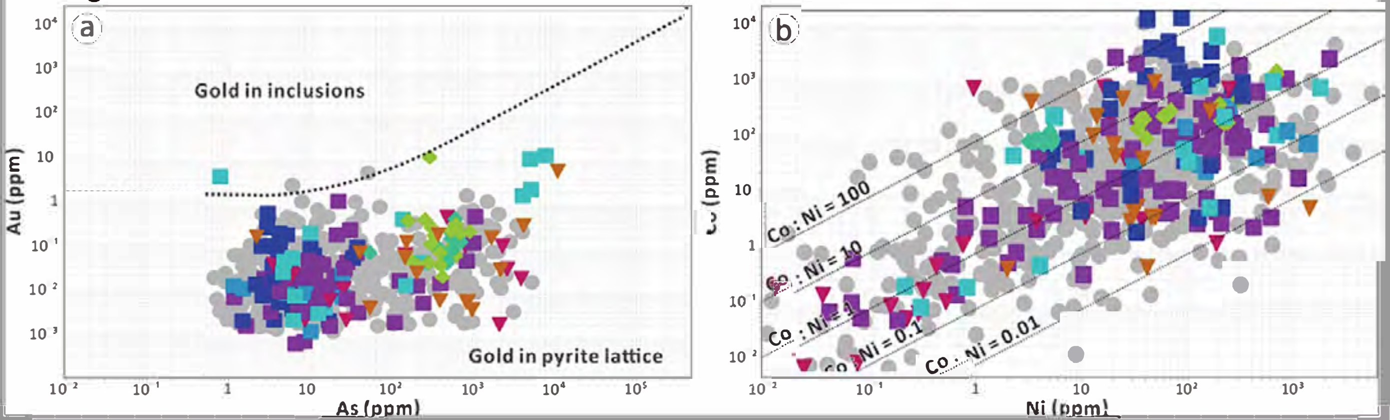

a
Gold in inclusions
Gold in pyrite lattice
Au (ppm)
As (ppm)
b
Co : Ni = 100
Co : Ni = 10
Co : Ni = 0.1
Co : Ni = 0.01
Ni (ppm)

Fig. 10

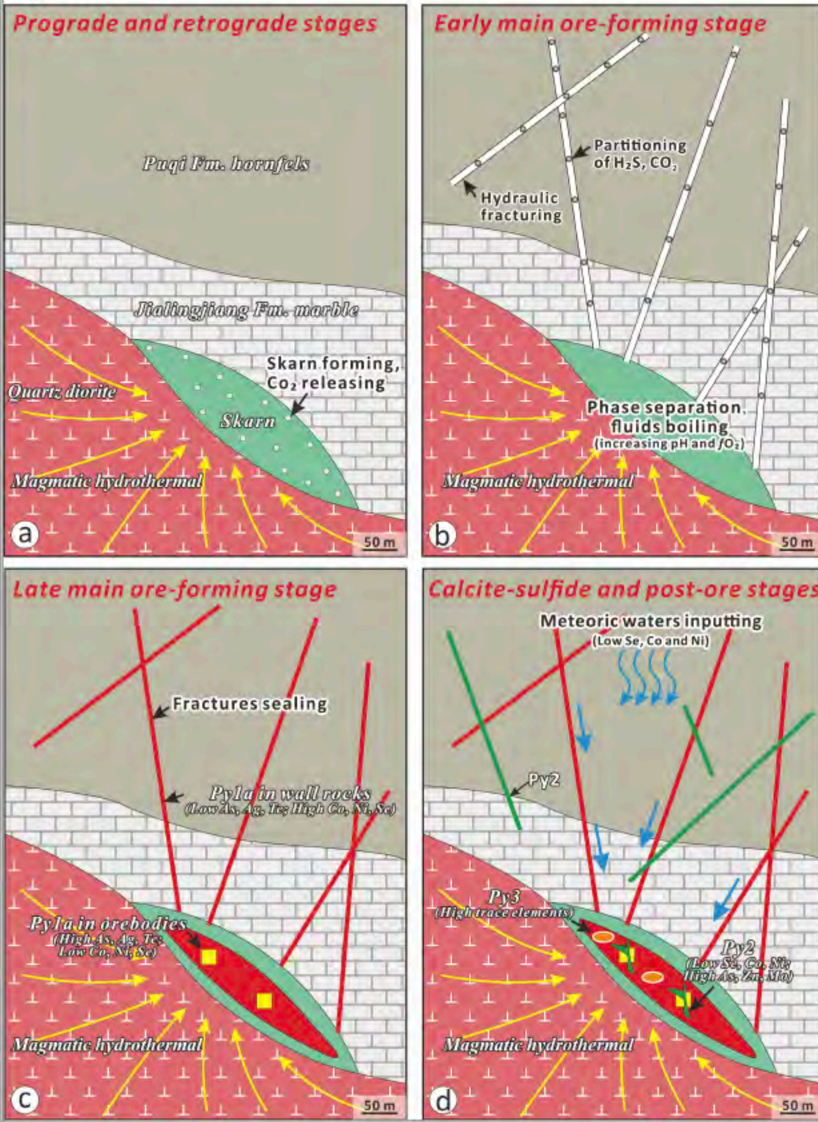

Prograde and retrograde stages
Puqi Fm. hornfels
Jialingjiang Fm. marble
Skarn forming, Co$_2$ releasing
Quartz diorite
Skarn
Magmatic hydrothermal
a
50 m
Early main ore-forming stage
Partitioning of H_2S, CO_2
Hydraulic fracturing
Phase separation, fluids boiling
(increasing pH and fO_2)
Magmatic hydrothermal
b
50 m
Late main ore-forming stage
Fractures sealing
Py1a in wall rocks
(Low As, Ag, Te; High Co, Ni, Se)
Py1a in orebodies
(High As, Ag, Te; Low Co, Ni, Se)
Magmatic hydrothermal
c
50 m
Calcite-sulfide and post-ore stages
Meteoric waters inputting
(Low Se, Co and Ni)
Py2
Py3
(High trace elements)
Py2
(Low Se, Co, Ni; High As, Zn, Mo)
Magmatic hydrothermal
d
50 m

Fig. 11

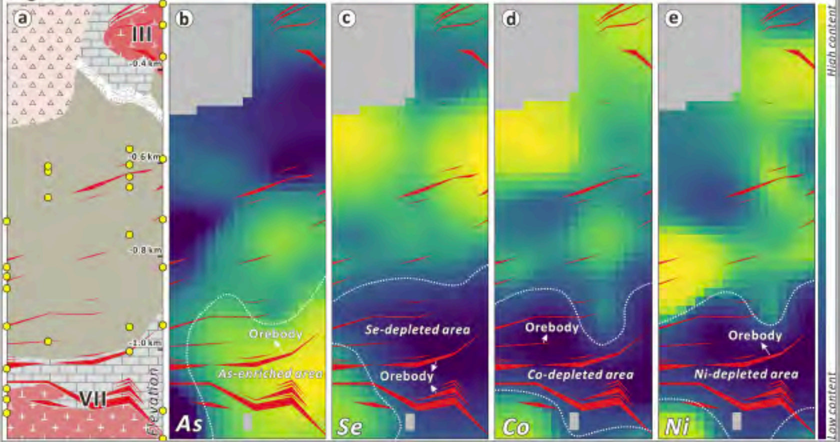
a
III
-0.4 km
-0.6 km
-0.8 km
-1.0 km
VII
Elevation
b
Orebody
As-enriched area
As
c
Se-depleted area
Orebody
Se
d
Orebody
Co-depleted area
Co
e
Orebody
Ni-depleted area
Ni
High content
Low content